Bachelor's Thesis

Simulating the Cooling Processes in the Evolution of Dark Matter Minihalos and Miniquasars using Grackle

Finn Karstens

Submitted on December 2, 2024

Institute for Theoretical Physics
Max-von-Laue-Str. 1
60438 Frankfurt, Germany

Supervisor and First Examiner
Prof. Dr. Laura Sagunski
Institute for Theoretical Physics
Goethe University Frankfurt,
Germany

Second Examiner
Prof. Dr. Sean Tulin
Department of Physics and
Astronomy
York University Toronto, Canada

Contents

1 Introduction

1.1 Motivation and Scientific Context

The early universe was a dynamic and complex environment where dark matter and gas worked together to form the first structures. Dark matter minihalos, which are gravitationally bound objects, were among the first building blocks of cosmic structure. These early structures often hosted miniquasars, small-scale versions of quasars powered by black holes. These miniquasars emitted intense radiation that heated and ionized the gas within and around the minihalos, affecting how new structures formed.

Dark matter played a crucial role in shaping the early universe, influencing the formation of gravitational potential structures within minihalos. These potentials guided the behavior of gas, contributing to the creation of the first cosmic structures. The interaction between dark matter dynamics and the thermal evolution of gas is an important area of study, particularly for understanding the conditions that led to the formation of the first stars.

Numerical simulations allow for the detailed modeling of gas dynamics and radiative transfer in complex astrophysical environments. The Grackle library, a popular tool for modeling radiative cooling and chemical processes, is ideal for studying how minihalos evolved. By including both heating and cooling processes, Grackle helps to investigate how these mechanisms shape the early universe.

1.2 Objectives of the Study

This thesis focuses on investigating the heating and cooling processes within a minihalo influenced by a central miniquasar. The study aims to model how radiative and collisional processes impact the thermal evolution of the gas and to

provide detailed cooling and heating rates that can be used for simulating the development of minihalos.

The work specifically explores various radiative cooling mechanisms in minihalos, such as collisional excitation and recombination cooling, along with heating processes like photoelectric heating.

Additionally, this thesis investigates the influence of key physical parameters, including gas density, far ultraviolet radiation (FUV) intensity (G_0), and internal energy, on the calculated cooling rates. These parameter studies help to refine the understanding of how different conditions within a minihalo affect its thermal state. The final goal is to generate accurate cooling and heating rates for simulating a minihalo, offering insights into the processes shaping the early universe.

1.3 Methodology

The methodology of this thesis is based on numerical simulations using the Grackle library. Grackle provides a framework for solving the chemical and thermal equations that describe the behavior of primordial gas. This study uses a reduced chemical network that includes six key species: neutral hydrogen (HI), ionized hydrogen (HII), neutral helium (HeI), singly ionized helium (HeII), doubly ionized helium (HeIII), and electrons (e^-).

The implementation involves initializing a fluid container that represents the physical and chemical properties of the gas. A key focus is on the calculation of the cooling rate (Λ) and heating rate Γ.

1.4 Structure of the Thesis

This thesis is organized into five chapters to provide a good understanding of the research. Chapter 2 outlines the essential concepts related to dark matter, minihalos, and miniquasars. It also explains the various cooling and heating processes that occur within minihalos. Chapter 3 introduces the Grackle library, detailing how it is used to simulate the thermal and chemical behavior of gas in a minihalo. The chapter also explains the parameters and settings chosen for calculating

the cooling and heating rates. Chapter 4 presents and analyzes the outcomes of the simulations, focusing on how key inputs such as internal energy, gas density, and FUV radiation intensity (G_0) affect the cooling and heating rates. Chapter 5 summarizes the key findings and provides a perspective on future work.

2 Theoretical Background

2.1 Dark Matter and Minihalo Formation

2.1.1 The Role of Dark Matter

Dark matter is a key component of the universe, making up about 85% of all matter and 27% of the universe's total energy, according to the 2018 Planck mission results [1]. It interacts through gravity and is invisible because it does not emit, reflect, or absorb light. This means dark matter can only be detected indirectly by its gravitational effects. Its abundance and gravitational influence are essential for forming and shaping cosmic structures like galaxies, galaxy clusters, and the cosmic web.

The existence of dark matter is supported by many observations. One well-known example is the rotation curves of galaxies, studied in the 1970s by Vera Rubin [2]. In the outer regions of galaxies, stars and gas rotate faster than expected based on visible matter alone. This discrepancy indicates additional, unseen mass, what we call dark matter [2].

Gravitational lensing provides a further indication. When light from distant objects passes near massive objects, like galaxy clusters, it bends due to gravity. Observations of galaxy clusters, such as Abell 1689, show that visible matter alone cannot explain the strength of these lensing effects. In these cases, dark matter accounts for most of the mass and amplifies the lensing effects [3].

The cosmic microwave background (CMB) also reveals the impact of dark matter. Fluctuations in the CMB's radiation density were influenced by dark matter's gravitational potentials before normal matter (baryons) could settle into these potentials. The precise measurements from the Planck mission offer insights into dark matter's role in the early universe [1].

A significant simulation showcasing dark matter's role in structure formation is the Millennium Simulation, based on the Cold Dark Matter (CDM) model. CDM describes dark matter as slow-moving (non-relativistic), collisionless particles. These particles gravity enables the growth of density fluctuations in the early universe, leading to large-scale structures like galaxy clusters [4].

The Millennium Simulation, conducted by Springel et al. (2005), models how these structures evolve. It shows how dark matter forms the cosmic web and pulls ordinary matter into its gravitational wells, leading to stars, galaxies, and galaxy clusters.

The results are shown in Figure 2.1. The upper panels display the distribution of galaxies and their light (left: detailed view, right: large-scale distribution). These distributions align closely with the underlying dark matter shown in the lower panels. Dark matter serves as the foundation of structures, shaping the distribution of visible baryonic matter.

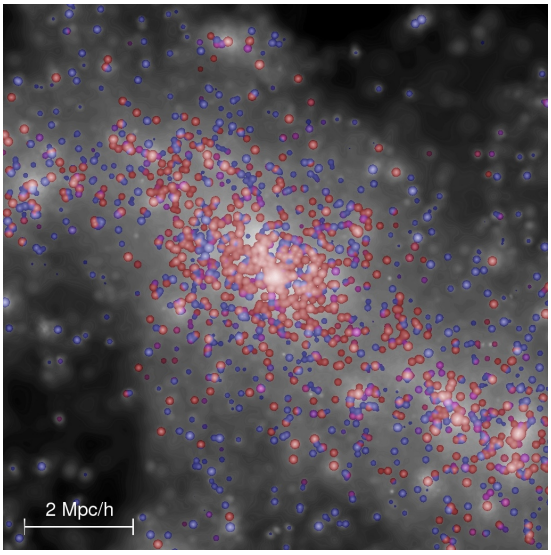

(a) Detailed view of the galaxy distribution on large scales with a length scale of 2Mpc/h. The light distribution shows the position of individual galaxies and highlights the gravitational influence of the underlying dark matter.

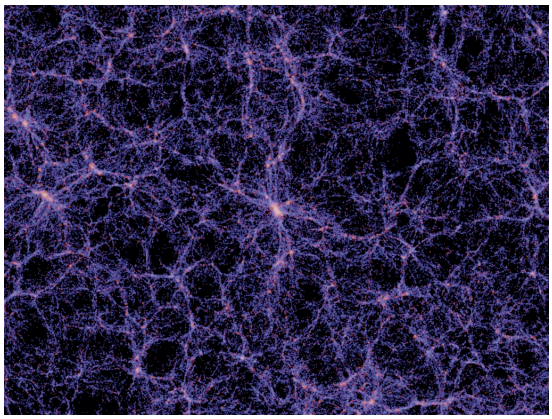

(b) Large-scale distribution of galaxies in the universe. This representation shows the light distribution of baryonic matter on very large scales and illustrates the large-scale structure of the universe.

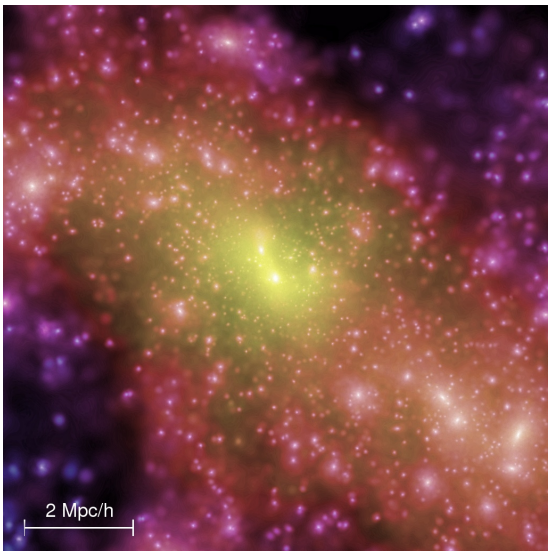

(c) Detailed view of the dark matter in the corresponding galaxy cluster from 2.1a.

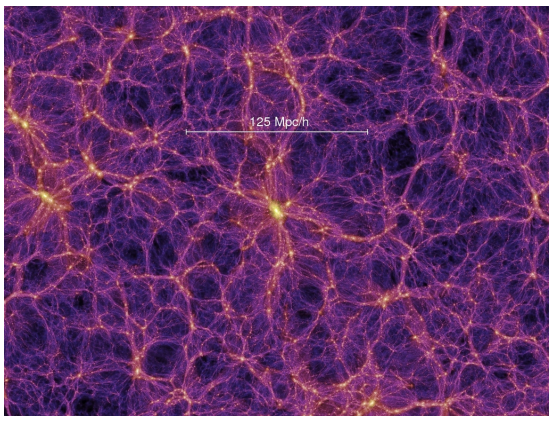

(d) Large-scale distribution of dark matter corresponding to 2.1b.

Figure 2.1: Visualizations from the Millennium Simulation show the link between dark matter and baryonic matter distributions. Adapted from [5].

Another model that differs from the CDM approach is Self-Interacting Dark Matter (SIDM). Dark matter halos are gravitational structures formed by the accumulation of dark matter and serve as the framework for galaxy formation. They usually contain a mixture of dark matter and baryonic matter, with dark matter being the dominant component. The SIDM model postulates elastic interactions between dark matter particles, which redistribute energy within these halos. This leads to the formation of flatter cores, in contrast to the steep cusps predicted by the CDM model. This phenomenon is known as the core-cusp problem and represents one of the major challenges for the CDM model.

The CDM halo density follows a Navarro-Frenk-White (NFW) profile:

$$\rho_{\mathrm{NFW}}(r) = \frac{\rho_0}{\frac{r}{r_s}\left(1+\frac{r}{r_s}\right)^2}. \tag{2.1}$$

The variables in this model are:

- $\rho_{\mathrm{NFW}}(r)$: The density of the halo as a function of the radius r.
- ρ_0: The characteristic density of the halo, which depends on the total mass of the halo and its concentration.
- r: The distance from the center of the halo.
- r_s: The scale radius of the halo, which defines the boundary between the inner and outer regions:
  - In the inner region ($r \ll r_s$), the density decreases with $\rho \propto r^{-1}$.
  - In the outer region ($r \gg r_s$), the density decreases more steeply with $\rho \propto r^{-3}$.

This profile describes a steep increase in density in the core region, leading to the so-called cusps [6]. In contrast, the SIDM model flattens the density due to elastic interactions, which is often described by an isothermal profile:

$$\rho_{\mathrm{SIDM}}(r) = \frac{\rho_c}{1+\left(\frac{r}{r_c}\right)^2}. \tag{2.2}$$

The variables in this model are:

- $\rho_{\text{SIDM}}(r)$: The density of the halo as a function of the radius r.
- ρ_c: The central density of the halo, which remains nearly constant in the core region ($r \ll r_c$).
- r: The distance from the center of the halo.
- r_c: The core radius, which describes the extent of the flat density region. For $r \gg r_c$, the density decreases similarly to the CDM model with $\rho \propto r^{-2}$.

The SIDM profile describes an almost constant density in the core region, consistent with observations of dwarf galaxies and other small structures that exhibit flat density cores [7].

Figure 2.2 illustrates this difference in the density profiles. The black line represents the steep NFW profile of CDM [6], while the colored lines show the flatter cores in SIDM models. SIDM is particularly relevant for smaller structures and offers a possible solution to discrepancies in observations [7, 8]. Additionally, Figure 2.2 shows the density distributions for different self-interaction strengths (σ/m). For $\sigma/m = 1\,\text{cm}^2/\text{g}$ (blue stars), the flattening is more pronounced than for $\sigma/m = 0.1\,\text{cm}^2/\text{g}$ (green triangles), highlighting the role of interaction strengths in shaping halos.

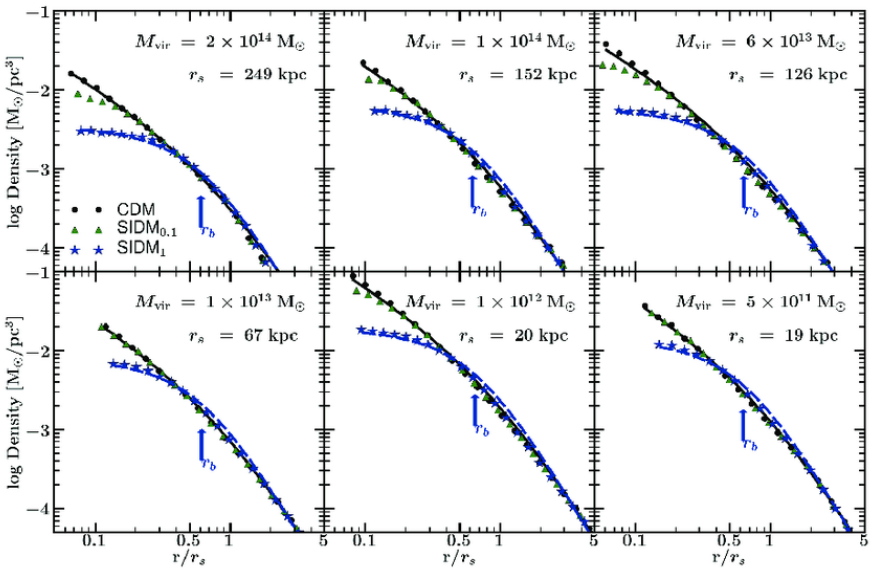

Figure 2.2: Comparison of the density profiles of CDM and SIDM. SIDM models show flatter cores due to self-interactions, while CDM predicts steep cusps. Adapted from: [8].

Another approach is dissipative dark matter, where energy is lost through dissipation. This loss of energy allows the inner regions of the halo to cool and contract faster, speeding up gravitational collapse. The halos formed in this way are more compact compared to those predicted by cold dark matter (CDM) or self-interacting dark matter (SIDM). [9].

Finally, warm dark matter (WDM) offers a moderate thermal velocity, suppressing small structures and resolving some discrepancies in CDM models. However, WDM struggles to explain larger structures [10].

Model	Properties	Interactions	Relevant Phenomena
Cold Dark Matter (CDM)	Non-relativistic, collisionless	Gravitational	Formation of large-scale structures, steep halo cores
Self-Interacting Dark Matter (SIDM)	Non-relativistic, elastic interactions	Gravitational, self-interacting	Flatter halo cores, solution to the core-cusp problem
Dissipative Dark Matter	Inelastic interactions, energy loss through radiation	Gravitational, self-interacting, dissipative	Accelerated halo collapse, more efficient gas accretion
Warm Dark Matter (WDM)	Moderate thermal velocity, lower mass	Gravitational	Suppression of small structures, delay in star formation

Table 2.1: Comparison of different dark matter models, including their properties, interactions, and relevant phenomena.

2.1.2 Formation and Evolution of Minihalos

Minihalos, small dark matter halos with typical masses of $10^5 - 10^6 M_\odot$, form during the cosmic dark ages. These early structures represent the first gravitationally bound objects in the universe and act as potential for baryonic matter. Their gravitational potentials enable the accumulation and cooling of gas, leading to the formation of dense baryonic cores [11, 12, 13]. These cores serve as the seeds for the formation of Population III stars, the universe's first stars. The supernovae of these stars enrich the gas with heavy elements, influencing the further evolution of minihalos [12]. Thus, minihalos play a crucial role in structure formation and form the foundation for the emergence of larger cosmic structures, such as galaxies and galaxy clusters. Figure 2.3 shows the cosmic timeline. Minihalos are pivotal

in the formation of the first stars and galaxies, which appeared approximately 10^7 to 10^8 years after the Big Bang [13, 11].

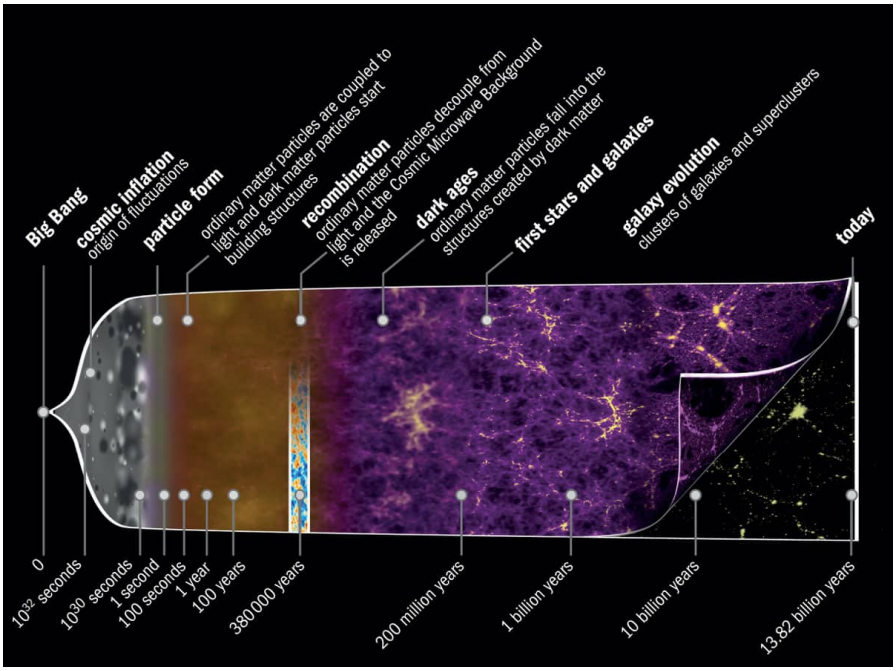

Figure 2.3: Cosmic timeline highlighting major events in the development of the universe. Minihalos emerge during the dark ages, marking the onset of structure formation in the universe. Adapted from: [14].

The first minihalos formed shortly after recombination, when the universe had cooled sufficiently for baryonic gas to decouple from the cosmic microwave background (CMB). The formation of minihalos can be divided into a linear and a nonlinear phase, describing their evolution from initial density fluctuations to compact gravitational potentials.

During the linear phase, initial density fluctuations, which originated from quantum fluctuations during inflation, grow slowly. The gravity of dark matter amplifies these fluctuations by pulling matter into denser regions [1]. In this phase, density fluctuations remain small ($\delta \ll 1$), and the processes proceed uniformly, without forming distinct structures like minihalos. However, this phase lays the foundation for subsequent nonlinear development. The growth of density fluctuations is mathematically described by the density contrast $\delta(r, t)$, as defined in Dodelson [15]:

$$\delta(r,t) = \frac{\rho(r,t) - \bar{\rho}(t)}{\bar{\rho}(t)}, \tag{2.3}$$

where $\delta(r,t)$ represents the relative density contrast, describing the deviation of the local density $\rho(r,t)$ from the mean density $\bar{\rho}(t)$ of the universe at a given time t.

When the density fluctuations become large enough ($\delta \gtrsim 1$), the nonlinear phase begins. During this phase, high-density regions collapse under their own gravity, forming compact minihalos. These structures provide gravitational potentials that can attract and accumulate baryonic gas [12]. During the collapse, the infalling gas is heated by compression but radiates energy, leading to the formation of dense baryonic cores. These cores enable the formation of the first Population III stars [11, 12] and mark the beginning of complex structure formation in the universe.

The dark matter model significantly influences both the structure and dynamics of minihalos formed during the nonlinear phase. Different dark matter models result in characteristic density profiles and physical processes within minihalos.

CDM halos follow the Navarro-Frenk-White profile (see Equation 2.1) and exhibit steep density cores, as shown in Figure 2.2. These halos dominate the large-scale structure of the universe and remain stable in the nonlinear phase because they lack internal interactions [6].

In SIDM halos, elastic interactions between dark matter particles allow for the redistribution of energy within the halo. This leads to a flattening of the density cores (see Equation 2.2 and Figure 2.2) and facilitates the accretion of baryonic gas [7]. The total energy within the halo remains conserved as no energy is lost, but rather redistributed among particles.

In contrast, dissipative interactions result in energy loss within the halo. This enhances compaction and causes the structures to shrink more efficiently, ultimately leading to the collapse of the minihalo. This process creates optimal conditions for the accumulation of baryonic gas [9].

2.2 Miniquasars: Properties and Formation

2.2.1 Definition and Basic Properties

Minihalos play a crucial role in the formation of miniquasars. Miniquasars are bright astrophysical objects that form as gas is pulled toward intermediate-mass black holes (IMBHs). They emerge in the universe's first minihalos, which serve as early centers of gravitational attraction, drawing in both baryonic matter and dark matter. These interactions establish the conditions necessary for miniquasars to form.

With typical luminosities of $L \sim 10^{42} - 10^{44}\,\mathrm{erg/s}$, miniquasars shine much brighter than normal stars but are not as bright as modern quasars or supermassive black holes [13, 12, 16]. These values are based on theoretical models and simulations that study how gas falls onto black holes and the radiation produced in early cosmic structures. Their radiation ranges from hard X-rays to UV light and directly affects the surrounding gas in the minihalo, ionizing and heating it [17, 18].

2.2.2 Conditions for Miniquasar Formation

The formation of miniquasars requires the presence of intermediate-mass black holes (IMBHs), which develop in the central regions of minihalos. These IMBHs, with typical masses ranging from 10^2 to $10^4\,M_\odot$, can form through different mechanisms. One possible scenario is direct collapse, where dense baryonic gas in minihalos collapses directly into massive black holes under certain conditions without intermediate stages. Such conditions occur when the gas cannot break apart into smaller fragments due to high temperatures or low metallicity. Another way IMBHs can form is from the remains of massive first-generation stars, known as Population III stars. After these stars end their lives as supernovae, they can leave behind black holes that grow by pulling in gas, eventually reaching the masses needed for IMBHs [13, 12]. However, not all IMBHs formed from Population III remains lead to the formation of miniquasars. To form a miniquasar, there must be enough gas falling into the black hole and efficient release of radiation.

Effective cooling processes are crucial for compressing the baryonic gas. Miniha-

los with masses of $M_{\text{Halo}} \sim 10^5 - 10^6 M_\odot$ provide the necessary conditions to form dense baryonic cores, which in turn lead to the creation of IMBHs. Differences in dark matter models affect how efficiently these processes occur, as discussed in Section 2.1.2.

2.2.3 Accretion Processes and Energy Output

The immense energy output of miniquasars comes from the accretion of gas onto intermediate-mass black holes. A rotating accretion disk forms around the black hole, where gravitational binding energy is converted into radiation. The efficiency of this process is described by the radiative efficiency ε_r, which typically has values of ~ 0.1 for miniquasars.

The luminosity of a miniquasar is given by the following equation [17]:

$$L_{BH}(t) = \varepsilon_r \dot{M}_{BH}(t) c^2, \tag{2.4}$$

where:

- $L_{BH}(t)$: The luminosity of the black hole at a given time t.
- ε_r: The radiative efficiency.
- $\dot{M}_{BH}(t)$: The accretion rate of gas onto the black hole.
- $c = 3 \times 10^5\,\text{km/s}$: The speed of light.

This equation shows that the energy output of a miniquasar depends strongly on the accretion rate $\dot{M}_{BH}(t)$. For a typical accretion rate of $0.01\,M_\odot$/year and an efficiency of $\varepsilon_r = 0.1$, the resulting luminosity is $L \sim 10^{44}\,\text{erg/s}$. Such radiation levels are enough to ionize the gas within the minihalo and influence the intergalactic medium on cosmic scales. [13, 12, 16]

In addition to the energy output, the radiation from a miniquasar also affects the surrounding gas. Radiation pressure and ionizing photons can heat the gas and suppress further accretion. At the same time, gas bubbles form around the IMBH, which can serve as signatures of early cosmic energy sources. Miniquasars play a key role in ionizing and heating the intergalactic medium during the reionization era.

2.3 Cooling and Heating Mechanisms in Minihalos

2.3.1 Cooling Rate

Under the primordial conditions present in early minihalos, the gas consists almost entirely of hydrogen and helium. The mass fraction of hydrogen X is approximately 0.75, while helium (Y) accounts for about 0.25 [1]. These primordial conditions significantly influence how efficiently the gas can cool since heavy elements or dust substances for cooling in later epochs are absent. In this environment, molecular hydrogen (H_2) acts as the main cooling agent, especially at temperatures below $10^4\,\mathrm{K}$, where atomic cooling becomes ineffective [11, 19]. The lack of metals and dust leads to unique cooling dynamics critical for the development of minihalos during the cosmic dark ages.

The rate at which gas cools can be mathematically expressed as:

$$\Lambda = \frac{E}{t_{\mathrm{cool}} \cdot \rho}, \tag{2.5}$$

where:

- Λ: the volumetric cooling rate ($\mathrm{erg\,s^{-1}\,cm^{-3}}$),
- E: the specific thermal energy of the gas ($\mathrm{erg\,g^{-1}}$),
- t_{cool}: the characteristic time it takes for the gas to cool (s),
- ρ: the gas density ($\mathrm{g\,cm^{-3}}$).

This equation shows the relationship between the thermal energy, the density of the medium, and the time required for the gas to radiate its energy. For a given density, higher thermal energy leads to faster cooling, while lower density makes the process slower [20].

At the same time, external or internal heating, described by the volumetric heating rate Γ, can partially or fully offset cooling. In minihalos, Γ plays a crucial role, as radiation sources like miniquasars can add heat energy to the gas. The balance between Λ and Γ determines the thermal state of the gas:

$$\frac{\mathrm{d}E}{\mathrm{d}t} = \Gamma - \Lambda. \tag{2.6}$$

If $\Gamma > \Lambda$, the gas heats up, while cooling occurs when $\Gamma < \Lambda$.

The chemical network in minihalos includes primordial species such as neutral hydrogen (H), ionized hydrogen (H^+), electrons (e^-), molecular hydrogen (H_2), and the various helium species (He, He^+, He^{++}). These species are involved in chemical reactions that affect both the cooling and heating of the gas.

2.3.2 H_2 Charge Exchange, Three-Body Formation, and Molecular Cooling

In minihalos, molecular hydrogen (H_2) is an important substance for cooling at low temperatures below 10^4 K, where atomic processes like cooling by ionized atoms become inefficient. H_2 helps the gas lose energy through rotational and vibrational transitions, reducing its temperature and affecting gas dynamics. The formation and cooling by H_2 are closely connected and depend on chemical reactions and thermodynamic conditions.

A key process for the creation of H_2 is the reaction between negatively charged hydrogen (H^-) and neutral hydrogen (H):

$$H^- + H \rightarrow H_2 + e^- \tag{2.7}$$

This mechanism is the main way H_2 is created under primordial conditions, as heavier elements that help molecule formation in later epochs are absent. The reaction rate coefficient for this process, $k_{11}(T)$, depends on the temperature and is given by the following equation, specified in [21]:

$$k_{11}(T) = \exp\left(-\frac{a}{T}\right) \sum_{i=0}^{7} b_i (\ln T)^i, \tag{2.8}$$

where:

- T: the temperature in Kelvin,
- a: the activation energy,
- b_i: the coefficients of a polynomial expansion based on experimental and theoretical data.

In dense regions, especially at densities above $10^{10}\,\mathrm{cm}^{-3}$, three-body reactions are the main way H_2 forms. These reactions are highly effective and quickly turn atomic hydrogen into molecular hydrogen. The main mechanism is:

$$H + H + H \rightarrow H_2 + H \tag{2.9}$$

The effectiveness of this reaction depends heavily on the temperature and the rate coefficients used. Studies such as Abel et al. (2002) [22], Palla et al. (1983) [23], and Glover (2008) [24] have proposed different formulas for these rates. These differences can lead to variations in simulation results, as shown by Turk et al. (2011) [25]. In addition to forming H_2, three-body reactions also release heat, adding about 4.48 eV per H_2 molecule formed. This added heat can affect the balance between cooling and other processes, influencing gas fragmentation and collapse.

Once H_2 is formed, molecular cooling helps balance the energy. Rotational and vibrational transitions in H_2 are caused by collisions between H_2 and neutral hydrogen (H). These transitions emit photons, which remove energy from the gas. The rates for these processes are based on quantum mechanical calculations of cross-sections ($\sigma_{vj\rightarrow v'j'}$) and are described by [26] as:

$$k_{vj\rightarrow v'j'}(T) = \left(\frac{8}{\pi\mu k_B^3 T^3}\right)^{1/2} \int_0^\infty \sigma_{vj\rightarrow v'j'}(E_c) E_c e^{-E_c/k_B T} dE_c, \tag{2.10}$$

where:

- μ: the reduced mass of the H_2-H system,
- k_B: the Boltzmann constant,
- E_c: the kinetic energy of the collision,
- T: the temperature in Kelvin,
- $\sigma_{vj\rightarrow v'j'}(E_c)$: the cross-section for the transition from the initial state (v, j) to the final state (v', j').

This cooling works best in the temperature range $100\,\mathrm{K} \leq T \leq 5000\,\mathrm{K}$, where rotational and vibrational transitions are most active. At temperatures below 100 K, the rates become very small because collisions happen less often.

Cooling by H_2 depends directly on the amount of H_2, the amount of neutral hydrogen (H), and the temperature-based rates. This can be summarized as:

$$\Lambda_{H_2} \propto n_{\mathrm{H_2}} n_H k(T), \tag{2.11}$$

where:

- Λ_{H_2}: the volumetric cooling rate ($\mathrm{erg\,s^{-1}\,cm^{-3}}$),
- $n_{\mathrm{H_2}}$ and n_H: the particle densities of H_2 and H,
- $k(T)$: the rates that depend on temperature.

The rate coefficient $k(T)$ includes how efficiently H_2 forms and its rotational and vibrational transitions. These processes help the gas lose energy and reduce its temperature.

2.3.3 Collisional Excitation Cooling

In collisional excitation, electrons collide with atoms or ions, exciting them to higher energy levels. These excited particles return to their ground state by emitting photons, releasing energy as radiation. This process is a key mechanism for cooling the gas and influences the thermal evolution of the environment.

The volumetric cooling rate Λ_{exc}, which is the energy radiated per unit volume, can be expressed as:

$$\Lambda_{\mathrm{exc}} = n_e n_1 q_{12}(T) h\nu_{21}, \tag{2.12}$$

(from Equation 3.22 in [27]). Here:

- n_e: the electron density,
- n_1: the number density of particles in the lower energy level,
- $q_{12}(T)$: the temperature-dependent collision rate coefficient,

- $h\nu_{21}$: the energy of the transition between levels 2 and 1.

This equation shows that cooling is proportional to the particle density and the excitation rate.

The collision rate coefficient $q_{12}(T)$ is determined by the Maxwell-Boltzmann distribution of electron speeds and can be expressed as:

$$q_{12}(T) = 8.629 \times 10^{-6} \frac{\Upsilon(1,2)}{\omega_1 T^{1/2}} e^{-\chi/kT}, \tag{2.13}$$

(from Equation 3.20 in [27]). Here:

- $\Upsilon(1,2)$: the averaged collision strength,
- χ: the excitation potential,
- ω_1: the statistical weight of the lower energy level,
- T: the temperature, and
- k: the Boltzmann constant.

The averaged collision strength $\Upsilon(1,2)$ is calculated from the quantum mechanical cross-sections $\sigma_{12}(u)$, given by:

$$\sigma_{12}(u) = \frac{\pi\hbar^2}{m^2 u^2} \Omega(1,2), \tag{2.14}$$

(from Equation 3.14 in [27]), where:

- $\Omega(1,2)$: the collision-specific strength, depending on the speed and energy of the collision.

The efficiency of collisional excitation cooling strongly depends on the particle density. Below a critical density $n_c(i)$, radiative de-excitation dominates, while at higher densities, collisional de-excitation becomes more significant. The critical density is given by:

$$n_c(i) = \frac{\sum_j A_{ij}}{\sum_k q_{ij}}, \tag{2.15}$$

(from Equation 3.30 in [27]), where:

- A_{ij}: the transition probability for radiative de-excitation,
- q_{ij}: the rate coefficients for collisional transitions.

In low-density environments, the cooling rate scales linearly with $n_e n_1$, while at high densities, it decreases.

Temperature also plays an important role in cooling efficiency. At low temperatures, excitation is suppressed by the Boltzmann factor $e^{-\chi/kT}$, reducing cooling. At high temperatures, the likelihood of excitation increases, but at very high energies, the collision strength saturates, and the cooling rate levels off [27].

An example is cooling by hydrogen. The key transition is the excitation from $2S \rightarrow 2P$, followed by the emission of a Lyman-α photon with an energy of 10.2 eV. For helium, similar processes occur between different energy levels [27].

2.3.4 Collisional Ionization Cooling

Collisional ionization occurs when fast electrons transfer enough energy through collisions with neutral atoms or ions to eject bound electrons. Ionization contributes to the cooling of the gas by using the excess kinetic energy of the electrons for ionization, which reduces the thermal energy of the system. The effectiveness of this process depends on the temperature and the abundance of the involved atoms and electrons.

The volumetric cooling rate for electron-impact ionization can be described similarly to collisional excitation cooling. The general form is:

$$\Lambda_{\text{ion}} = n_e n_{\text{H}} q_{\text{ion}}(T) E_{\text{ion}}, \tag{2.16}$$

where:

- n_e: the electron density,
- n_{H}: the density of neutral hydrogen atoms,
- $q_{\text{ion}}(T)$: the temperature-dependent ionization rate coefficient,
- E_{ion}: the ionization energy in eV.

The ionization rate $q_{\text{ion}}(T)$ is determined by the Maxwell-Boltzmann distribution of electron velocities and can be expressed as:

$$q_{\text{ion}}(T) = 8.629 \times 10^{-6} \frac{\Upsilon_{\text{ion}}}{T^{1/2}} \exp\left(-\frac{E_{\text{ion}}}{kT}\right) \tag{2.17}$$

where:

- Υ_{ion}: the temperature-dependent collision strength for ionization,
- E_{ion}: the ionization energy (e.g., 13.6 eV for hydrogen),
- T: the temperature in Kelvin,
- k: the Boltzmann constant.

In minihalos, the primary ionization energies are for hydrogen (H) and helium (He). For hydrogen, $E_{\text{ion}} = 13.6\,\text{eV}$, while helium has two ionization stages with energies of 24.6 eV and 54.4 eV. The total cooling rate is calculated by summing the contributions from all species.

2.3.5 Recombination Cooling

Electrons lose kinetic energy when they recombine with ions. This energy is emitted as radiation, which contributes to cooling the gas. Recombination cooling is particularly important in ionized regions.

The volumetric cooling rate for recombination in hydrogen $\Lambda_{\text{rec}}(H)$ is given by:

$$\Lambda_{\text{rec}}(H) = n_e n_p kT \beta_A(H^0, T), \tag{2.18}$$

(from Equation 3.3 in [27]). Here:

- n_e: the electron density,
- n_p: the proton density,
- T: the temperature,
- k: the Boltzmann constant,

- $\beta_A(H^0, T)$: the temperature-dependent recombination coefficient.

The term $\beta_A(H^0, T)$ is the sum of the recombination rates for all energy levels:

$$\beta_A(H^0, T) = \sum_{n=1}^{\infty} \beta_n(H^0, T), \tag{2.19}$$

(from Equation 3.4 in [27]), where n is the principal quantum number of the target energy level for the recombining electron.

The calculation of $\beta_n(H^0, T)$ is based on the recombination cross-section $\sigma_{nL}(H^0, T)$, averaged over the kinetic energy:

$$\beta_n(H^0, T) = \frac{1}{kT} \int_0^{\infty} u\sigma_{nL}(H^0, T)\frac{1}{2}mu^2 f(u)\, du, \tag{2.20}$$

(from Equation 3.5 in [27]). Here:

- u: the electron velocity,
- m: the electron mass,
- $f(u)$: the Maxwell-Boltzmann distribution of electron velocities.

For helium-rich regions, the volumetric cooling rate for helium is calculated similarly:

$$\Lambda_{\text{rec}}(He) = n_e n(He^+) kT \beta_A(He^0, T), \tag{2.21}$$

(from Equation 3.13 in [27]), where $n(He^+)$ is the density of singly ionized helium ions.

The total recombination cooling rate is then given by:

$$\Lambda_{\text{rec}} = \Lambda_{\text{rec}}(H) + \Lambda_{\text{rec}}(He), \tag{2.22}$$

(from Equation 3.12 in [27]). This equation shows that recombination cooling is proportional to the densities of ions and electrons.

2.3.6 Bremsstrahlung Cooling

Bremsstrahlung cooling is an important mechanism in ionized gases, occurring when free electrons interact with ions. The electrons lose energy in the form of

continuous electromagnetic radiation as they are deflected near ions.

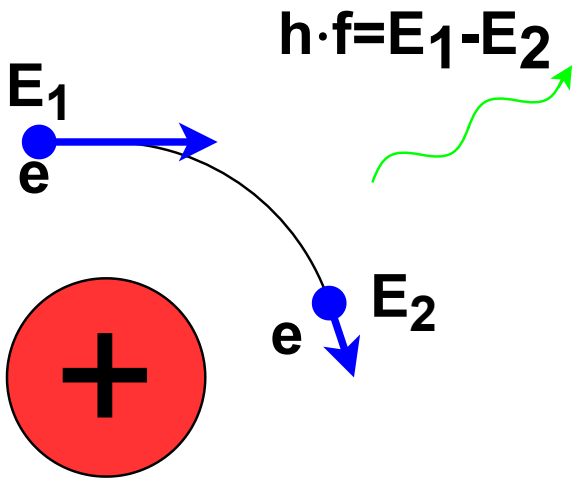

Figure 2.4: Illustration of Bremsstrahlung radiation.

This process is particularly significant in hot, diffuse environments.

The volumetric cooling rate due to Bremsstrahlung for ions with charge Z is given by:

$$\Lambda_{\text{bre}}(Z) = 4\pi j_{ff}, \tag{2.23}$$

(from Equation 3.4 in [27]), where j_{ff} is the free-free emission rate. This rate can be approximately expressed as:

$$j_{ff} = \frac{2^5 \pi e^6 Z^2}{3^3 hmc^3} \left(\frac{2\pi kT}{m}\right)^{1/2} g_{ff} n_e n_+, \tag{2.24}$$

(from Equation 3.4 in [27]). Here:

- e: the elementary charge,
- h: Planck's constant,

- m: the electron mass,
- c: the speed of light,
- k: the Boltzmann constant,
- T: the temperature,
- g_{ff}: the Gaunt factor,
- n_e: the electron density,
- n_+: the ion density.

The cooling rate can then be summarized as:

$$\Lambda_{\text{bre}}(Z) = 1.42 \times 10^{-27} Z^2 T^{1/2} g_{ff} n_e n_+ \, [\text{erg cm}^{-3}\text{s}^{-1}], \tag{2.25}$$

(from Equation 3.4 in [27]).

The ion density n_+ is primarily dominated by H^+, as protons are the most abundant ions in ionized environments like minihalos. The Gaunt factor g_{ff} is a weakly varying function of n_e and T, typically in the range $1.0 < g_{ff} < 1.5$.

Bremsstrahlung cooling is particularly important in high-temperature environments, as the emission rate scales with $\sqrt{T}$. Unlike recombination cooling, this process does not rely on the presence of neutral atoms or ions and can occur in fully ionized regions, making it a dominant cooling mechanism.

2.3.7 Photoelectric Heating

Photoelectric heating occurs when high-energy ultraviolet (FUV) radiation ejects electrons from atoms or molecules. These freed electrons transfer energy to the gas, causing its temperature to rise. The volumetric heating rate Γ, which describes the energy added per unit volume and time, is given by:

$$\Gamma = 1.0 \times 10^{-24} n_e \epsilon G_0 \quad [\text{erg cm}^{-3}\ \text{s}^{-1}], \tag{2.26}$$

(adapted from [28]). Here:

- n_e: the electron density [cm^{-3}],
- ϵ: the photoelectric heating efficiency,
- G_0: the strength of the incoming FUV radiation field, normalized to the Habing unit (1.6×10^{-3} erg s^{-1} cm^{-2}).

The efficiency ϵ represents the fraction of absorbed FUV radiation converted into heat. It depends on physical conditions such as gas density, temperature, and the radiation intensity G_0. The efficiency is calculated using the following relation [28]:

$$\epsilon = \frac{4.9 \times 10^{-2}}{1.0 + \left(\frac{G_0 T^{1/2}/n_e}{1925}\right)^{0.73}} + \frac{3.7 \times 10^{-2} \left(\frac{T}{10^4}\right)^{0.7}}{1.0 + \left(\frac{G_0 T^{1/2}/n_e}{5000}\right)} \tag{2.27}$$

This equation shows that ϵ is highest at low radiation intensities G_0, low temperatures T, and high electron densities n_e, while it decreases at high values of $G_0 T^{1/2}/n_e$.

In minihalos, the FUV radiation typically originates from a central miniquasar, which influences the gas within the halo through radiation. The value of G_0 directly depends on the intensity of radiation emitted by the miniquasar.

3 Methodology

3.1 Dark Matter Model

For this study, a dissipative dark matter model was chosen because it more realistically represents physical processes on small scales and provides new insights into the formation of miniquasars.

While the standard Cold Dark Matter (CDM) model describes minihalos as gravitational centers that attract gas and serve as the foundation for the first stars and black holes, our approach extends this concept by considering dark matter as collisional and dissipative. In our model, dark matter particles interact and lose energy through dissipative processes, allowing minihalos to collapse more rapidly. This accelerates the formation of intermediate-mass black holes.

The dissipative dark matter model accounts for energy losses, leading to stronger density concentrations in the central regions and the eventual collapse of minihalos. This creates optimal conditions for the accretion of baryonic gas. In contrast, CDM predicts steep density cusps, while Self-Interacting Dark Matter (SIDM) produces flatter cores that do not achieve the high densities of halo cores seen in the dissipative model.

A key advantage of this model is its realistic representation of the interaction between dark matter and gas. This interaction is crucial for the formation of miniquasars, as it influences the growth of black hole masses and the luminosity of the miniquasars.

3.2 Grackle Library

To model the physical processes in minihalos realistically and efficiently, a suitable numerical library is needed. For this work, the Grackle Library was used,

a versatile open-source tool specifically designed for simulating cooling processes, chemical reactions, and thermal evolution in cosmological environments.

Minihalos, composed of dark matter and primordial gas, require accurate modeling of the thermal and chemical processes that influence their evolution. These include radiative cooling processes such as recombination cooling, bremsstrahlung cooling, and collisional ionization cooling, as well as heating mechanisms like photoelectric heating from radiation. Additionally, Grackle models the chemical evolution of primordial gas, primarily composed of hydrogen and helium, accounting for important processes.

One significant advantage of Grackle is its flexibility. The library allows specific heating and cooling processes to be selectively activated or deactivated to fit various astrophysical scenarios. This flexibility enables targeted simulations of thermodynamic effects in minihalos. Moreover, user defined parameters, such as the intensity of the interstellar radiation field G_0—dominated by a central miniquasar in the case of a minihalo—can be easily adjusted.

Additionally, Grackle integrates easily with various simulation environments. Its Python interface, Pygrackle, simplifies access to all Grackle's features, making implementation and usage much easier.

Another reason for choosing Grackle is its open-source nature. The library is continuously updated by an active scientific community, ensuring that its underlying models meet the latest scientific standards. Grackle's open-source approach allows for broad validation by the research community and ensures efficiency, which is essential for large-scale simulations like those conducted in this study.

3.3 Parameter Selection

3.3.1 Primordial Chemistry

For the chemical modeling in this study, the parameter *primordial_chemistry* was set to 1. This activates a chemical network that includes the fundamental species and reactions in primordial gas. The modeled species are neutral hydrogen (H), ionized hydrogen (H^+), electrons (e^-), and helium in its neutral (He), singly ionized (He^+), and doubly ionized (He^{++}) forms. The chemical reactions occurring

between these species are detailed in Table 3 in [29] (Figure 3.1).

$$
\begin{aligned}
\mathrm{H} + \mathrm{e}^- &\rightarrow \mathrm{H}^+ + \mathrm{e}^- + \mathrm{e}^- \\
\mathrm{H}^+ + \mathrm{e}^- &\rightarrow \mathrm{H} + \gamma \\
\mathrm{He} + \mathrm{e}^- &\rightarrow \mathrm{He}^+ + \mathrm{e}^- + \mathrm{e}^- \\
\mathrm{He}^+ + \mathrm{e}^- &\rightarrow \mathrm{He} + \gamma \\
\mathrm{He}^+ + \mathrm{e}^- &\rightarrow \mathrm{He}^{++} + \mathrm{e}^- + \mathrm{e}^- \\
\mathrm{He}^{++} + \mathrm{e}^- &\rightarrow \mathrm{He}^+ + \gamma \\
\mathrm{H} + \mathrm{H} &\rightarrow \mathrm{H}^+ + \mathrm{e}^- + \mathrm{H} \\
\mathrm{H} + \mathrm{He} &\rightarrow \mathrm{H}^+ + \mathrm{e}^- + \mathrm{He} \\
\mathrm{H} + \gamma &\rightarrow \mathrm{H}^+ + \mathrm{e}^- \\
\mathrm{He} + \gamma &\rightarrow \mathrm{He}^+ + \mathrm{e}^- \\
\mathrm{He}^+ + \gamma &\rightarrow \mathrm{He}^{++} + \mathrm{e}^-
\end{aligned}
$$

Figure 3.1: All allowed chemical reactions [29].

Additionally, the Grackle parameter *dust_chemistry* was disabled. This setting excludes all processes dependent on the presence of dust, such as the formation of molecular hydrogen (H_2) on dust grains, cooling by dust particles, and heat exchange between dust and gas. Since there are no metals or dust present in the environment of minihalos, these processes are irrelevant to this study. Disabling *dust_chemistry* reduces the complexity of the simulations and enables more efficient computations without compromising the physical relevance of the results.

It is important to note that Grackle implements additional physical processes such as H_2 charge exchange, three-body formation, and molecular cooling, which are not included in our specific chemical network (6-species model). Since our simulations focus on primordial conditions with a simplified chemical composition, these mechanisms are not significant for the results.

3.3.2 Heating and Cooling Processes in Grackle

The Grackle Library provides a comprehensive implementation of relevant heating and cooling processes required to model the thermodynamic evolution of minihalos. There are two main options for how Grackle handles these processes:

In the option *converge=False*, heating and cooling rates are calculated from tabulated equilibrium values, assuming a steady-state ionization balance. This mode is computationally more efficient since it only interpolates tabulated values but is less accurate for cases involving time-dependent effects or dynamic processes.

In the other option *converge=True*, an iterative approach is used where chemical species and heating and cooling rates are dynamically calculated until a convergence criterion is met. This mode allows for precise modeling of non-equilibrium processes and is better suited for scenarios where physical conditions change rapidly.

For our simulations, the *converge=True* mode was chosen as it provides a more realistic representation of the time-dependent evolution of heating and cooling rates and the chemical composition of the gas.

3.3.3 Collisional Excitation in Grackle

Grackle includes collisional excitation cooling, where the rates are based on tabulated data for excitation cross-sections and the Maxwell-Boltzmann distribution of electron velocities. The implementation follows standardized approaches for collisional excitation, as described in the works of Black (1981) [30] and Cen (1992) [31]. The code implementation aligns with the theoretical equation 2.12 for volumetric cooling rates, considering the density distribution of the participating species, including electrons, hydrogen (HI), and helium (HeI and HeII). Molecular processes, such as the excitation of H_2, are not included in the selected chemical network. [29]

3.3.4 Collisional Ionization in Grackle

Similarly, Grackle implements collisional ionization, where electrons transfer enough energy to ionize atoms by dislodging bound electrons. This increases the free electron density, which in turn enhances processes like recombination and bremsstrahlung

cooling. Cooling rates here are also based on tabulated ionization cross-sections and the Maxwell-Boltzmann distribution. The implementation follows standardized models described in the works of Shapiro & Kang (1987) [32], Cen (1992) [31], and Abel et al. (1997) [33]. It adheres to the theoretical equation 2.16 for volumetric cooling rates, taking into account the density distributions of electrons, hydrogen (HI), and helium (HeI and HeII). [29] External processes, such as ionization by photons, are not included in this process.

3.3.5 Recombination in Grackle

Grackle also calculates the volumetric cooling rate due to recombination, specifically for H^+, He^+, and He^{++}. [29] The implementation is based on a combination of theoretical models and tabulated values from studies like Black (1981) [30], Ferland et al. (1992) [34], and Hui & Gnedin (1997) [35]. These studies provide important parameters for the transition processes and the dependence of recombination cooling on temperature and electron density.

The numerical implementation in Grackle follows the approach described in Equation 2.22 for the volumetric cooling rate, which is applied iteratively to the involved species. The mean molecular weight is dynamically adjusted to precisely calculate the temperature and ionization balance. This is necessary because the cooling rate strongly depends on the ionization balance and the energy distribution of electrons.

By default, Grackle does not account for the optical depth of the recombined regions, which is not problematic for minihalos. However, for high-density regions or regions with significant metal abundance, the models may not be fully accurate.

3.3.6 Bremsstrahlung Cooling in Grackle

Grackle also implements Bremsstrahlung cooling. It uses an analytical approximation of the volumetric cooling rate for ionized gases. The cooling rate in Grackle is described by the following equation, similar to Equation 2.25:

$$\Lambda_{\text{bre}} = 1.42 \times 10^{-27}\, T^{1/2} \left[n(\text{H}^+) + n(\text{He}^+) + 4\, n(\text{He}^{++}) \right] n_e \tag{3.1}$$

where $n(H^+)$, $n(He^+)$, and $n(He^{++})$ are the densities of the ionized species, n_e is the electron density, and T is the temperature in Kelvin. This equation is derived from Black (1981) [30] and is valid for the temperature range $5 \times 10^3\,\mathrm{K} \leq T \leq 5 \times 10^8\,\mathrm{K}$, which covers the typical temperatures in minihalos.

In the implementation, the Gaunt factor (g_{ff}) is assumed to be weakly temperature-dependent and is set to a constant value of $g_{ff} \approx 1$ to simplify the calculations.

The implementation in Grackle accounts for all ionized species, including H^+, He^+, and He^{++}, with the higher efficiency of He^{++} represented by the factor of 4 in the equation. The cooling rate is calculated under the assumption that the gas is optically thin, which is a valid assumption for most regions within minihalos.

Molecular processes or other high-density effects, such as the formation of negative ions or molecules (e.g., H^-, H_2), are not considered in this approximation. These processes are not dominant in minihalos at the densities and temperatures considered, so they are neglected in this work. For low temperatures, such as those in our simulation, the results may become less accurate. However, since Bremsstrahlung cooling has only a minor impact on the cooling rate at low temperatures, this approximation is acceptable.

3.3.7 Photoelectric Heating in Grackle

Grackle has different methods to calculate photoelectric heating. In this work the method from Wolfire et al. (1995) [28] was used. The volumetric heating rate is modeled as described in Equation 2.26, using the efficiency ϵ from Equation 2.27.

In the implementation, a constant efficiency of $\epsilon = 0.05$ is assumed for temperatures below $20,000\,\mathrm{K}$ to effectively approximate the heating process in cool, dense regions. For temperatures above this value, $\epsilon = 0$ is set because the efficiency of electron release is negligible in these areas. [29]

The intensity of the far-ultraviolet (FUV) radiation G_0, which is determined by the luminosity of the central mini-quasar, plays a central role in the modeling. To determine the value of G_0 that Grackle requires as input, the following formula was used:

$$G_0 = \frac{L_0}{4\pi r^2} \cdot 1.0 \cdot 10^{-24}, [\mathrm{erg\ s^{-1}}, \mathrm{cm^{-2}}] \tag{3.2}$$

where L_0 is the total luminosity of the mini-quasar and r is the distance from the

quasar. The normalization factor $1.0 \cdot 10^{-24}$ scales the intensity to the Habing unit, which standardizes the radiation intensity.

The simplified modeling of the efficiency ϵ as constant below a certain temperature and negligible above it provides a good approximation that reduces the complexity of the calculations. This implementation is particularly suitable for minihalos, where the FUV radiation from the central mini-quasar dominates. For the conditions studied in this work, these assumptions are sufficiently accurate because the heating rate is mainly determined by G_0.

3.4 Implementation in Grackle

A Python wrapper for Grackle was used to simplify the implementation and customize the calculations to the specific needs of our mini-halo. Using a function to initialize the simulation system, a so-called Fluid Container is created, which contains the physical and chemical properties of the simulated gas, such as density, internal energy, and the concentration of various species.

The initialization is done by passing specific parameters, including the gas density, the internal energy (which is passed as an array), and the intensity of the FUV radiation G_0. The mass fractions of the chemical components are set through the parameters *hydrogen_mass_fraction* and *metal_mass_fraction*. For primordial gas, a hydrogen fraction of 76% and a metal fraction of 0.0 were chosen, as metals are not considered in our simulations. The deuterium-to-hydrogen ratio was also set to 0.0 to focus on a simplified primordial chemical network. The iteration to solve the chemical equilibrium is activated by *converge=True*, with the best possible tolerance for convergence chosen.

The calculations themselves are performed in an iterative loop that solves the chemical and thermodynamic processes of the system in discrete time steps. First, the cooling time for each cell is calculated, indicating the time period in which the gas loses its energy through cooling. The time step Δt is derived from the minimum cooling time, with a safety factor of 0.1 to ensure numerical stability. The chemical evolution of the system is then solved by the function *fc.solve_chemistry(dt)*, which updates the concentrations of the chemical species, taking into account reactions, heating, and cooling rates. During each iteration, the mean molecular weight of

the gas is calculated to ensure consistent temperature calculations.

A convergence check via the function *check_convergence()* ensures that the concentrations of the chemical species have stabilized within the defined tolerance. The check compares the concentrations of each species (HI, HII, HeI, HeII, HeIII, de) between two successive iterations and calculates the maximum relative deviation. This deviation is determined as the ratio of the absolute change to the previous concentration. Convergence is achieved when the maximum relative change for all species is smaller than the set tolerance. If the change for any species exceeds this tolerance, the iteration continues to further adjust the concentrations. After reaching convergence, the iteration is stopped; otherwise, it continues until the maximum number of iterations is reached. If convergence is not achieved, the script reports numerical instabilities.

At the end of the implementation, a function was developed that summarizes all the essential steps of initialization and cooling rate calculation. This function is responsible for initializing the Grackle chemical solver with the necessary input parameters, iteratively solving the chemical equilibrium, and finally calculating the cooling rate using Equation 2.5. The computed values, including the cooling rate, electron density, temperature, and so on, are returned in the desired units. A full grid of various values is pre-calculated for direct use in the mini-halo evolution simulation.

4 Results and Analysis

In this chapter, I present the results of my calculations, focusing on the cooling and heating processes within a minihalo under varying physical conditions. The goal is to investigate how key parameters, including gas density and the intensity of FUV radiation (G_0), affect cooling and heating rates. These results offer insights into the thermal and chemical evolution of gas within minihalos.

The chapter is organized into several sections. First, I discuss the behavior of various cooling mechanisms and identify their relative contributions.

Additionally, I examine the impact of varying gas densities and radiation intensities, with special attention to low-density regimes where Λ/ρ becomes density independent.

Next, I address extrapolations to regimes outside the directly simulated range in Grackle, including variations in density and temperature.

Finally, I compare the calculated rates with those reported in previous studies. This comparison provides context for evaluating the reliability and applicability of the findings to broader astrophysical scenarios.

4.1 Individual Cooling Rates

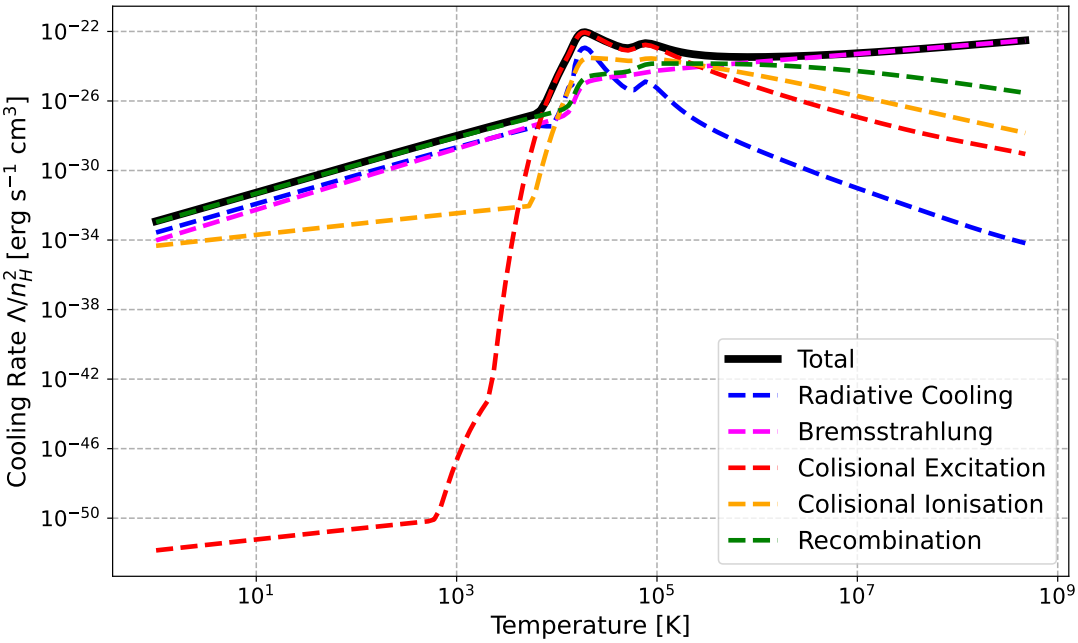

Figure 4.1: Individual cooling rates for $\rho = 10^6\,\mathrm{M}_\odot/\mathrm{kpc}^3$ & $G_0 = 0$. Each curve represents a specific cooling mechanism, highlighting its contribution across the temperature range.

Figure 4.1 illustrates the individual cooling rates for different processes at a gas density of $\rho = 10^6\,\mathrm{M}_\odot/\mathrm{kpc}^3$ and an FUV intensity of $G_0 = 0$. Each curve corresponds to a specific cooling mechanism, showing its contribution across the temperature spectrum.

At low temperatures (below $10^3\,\mathrm{K}$), recombination cooling dominates. This process is critical during the initial cooling stages, effectively reducing the gas energy.

In the intermediate temperature range ($10^4\,\mathrm{K}$ to $10^6\,\mathrm{K}$), collisional excitation is the primary contributor to the total cooling rate. The sharp peaks in this range are due to the excitation of atomic states, which subsequently emit photons as the states decay.

Collisional ionization also exhibits peaks in the intermediate temperature range, slightly offset from those of collisional excitation. These peaks indicate the role

of collisional processes in ionizing atoms, releasing free electrons and further contributing to cooling.

Radiative cooling, while present across all temperature ranges, does not dominate in any specific regime. It shows peaks at locations similar to those of collisional excitation and ionization, reflecting its dependence on atomic processes. However, its overall contribution remains secondary.

At high temperatures (above $10^6\,\mathrm{K}$), bremsstrahlung emerges as the dominant cooling mechanism. This is consistent with its strong temperature dependence and efficiency in highly ionized, hot environments.

The analysis of individual cooling rates provides a clear picture of the dominant processes at various temperatures, offering valuable insights into the thermal evolution of minihalos under primordial conditions.

4.2 Parameter Variation Analysis

4.2.1 Effect of Varying Densities

Figure 4.2 shows the cooling rate, Λ/n_H^2, in units of erg s^{-1} cm^3, and how it changes with gas density. At low densities, the cooling rate follows a nearly straight line and becomes linear for densities below $\rho = 10^{-3}\,\mathrm{M}_\odot/\mathrm{kpc}^3$. However, at very low energies, the cooling rate turns positive for these low densities. This happens because of a cosmic microwave background (CMB) temperature floor. To account for this, the cooling rate at T_{CMB} is subtracted from the total rate, which has minimal impact for higher densities.

For medium densities, between $\rho = 10^0\,\mathrm{M}_\odot/\mathrm{kpc}^3$ and $\rho = 10^{15}\,\mathrm{M}_\odot/\mathrm{kpc}^3$, the cooling rate shows two clear plateaus at specific energy ranges. These plateaus reflect key physical changes in the cooling processes. Interestingly, for densities from $\rho = 10^3\,\mathrm{M}_\odot/\mathrm{kpc}^3$ to $\rho = 10^{12}\,\mathrm{M}_\odot/\mathrm{kpc}^3$, the cooling rate curves look almost the same. This suggests that the physical mechanisms driving cooling in this range are very similar.

At very high densities, such as $\rho = 10^{15}\,\mathrm{M}_\odot/\mathrm{kpc}^3$ and $\rho = 10^{21}\,\mathrm{M}_\odot/\mathrm{kpc}^3$, the cooling rate increases dramatically by several orders of magnitude compared to lower densities. This is due to the much higher collision rates in these dense

conditions. However, at the highest density, $\rho = 10^{21}\,\mathrm{M}_{\odot}/\mathrm{kpc}^3$, the cooling rate slightly decreases at the highest energy values. This decrease suggests a saturation or weakening of certain cooling mechanisms under extreme conditions.

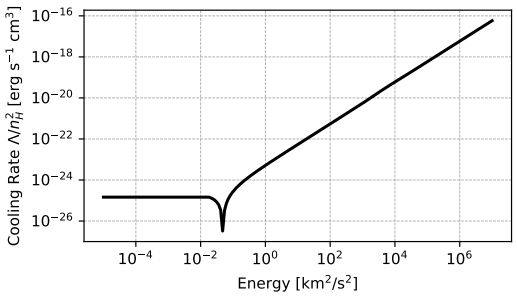

(a) $\rho = 10^{-3}\,\mathrm{M}_\odot/\mathrm{kpc}^3$ & $G_0 = 0$

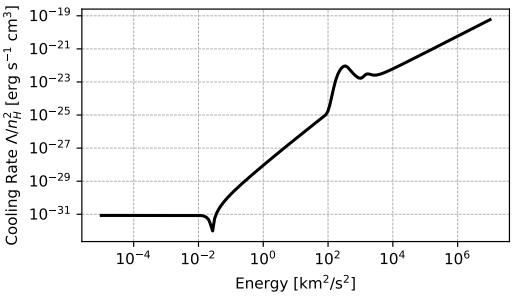

(b) $\rho = 10^{0}\,\mathrm{M}_\odot/\mathrm{kpc}^3$ & $G_0 = 0$

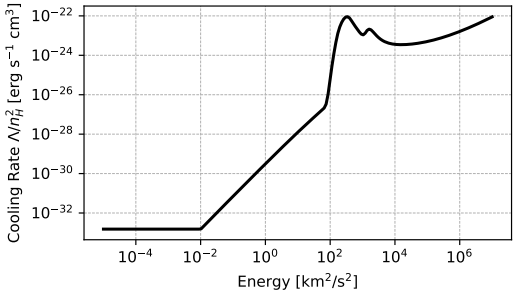

(c) $\rho = 10^{3}\,\mathrm{M}_\odot/\mathrm{kpc}^3$ & $G_0 = 0$

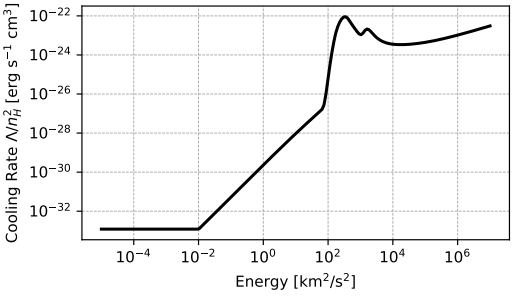

(d) $\rho = 10^{6}\,\mathrm{M}_\odot/\mathrm{kpc}^3$ & $G_0 = 0$

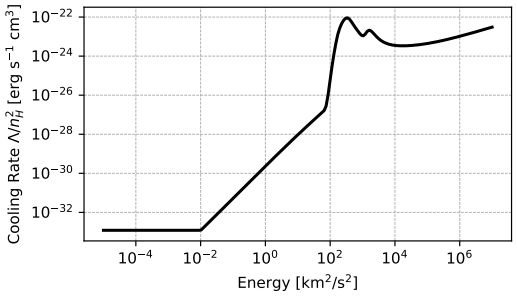

(e) $\rho = 10^{9}\,\mathrm{M}_\odot/\mathrm{kpc}^3$ & $G_0 = 0$

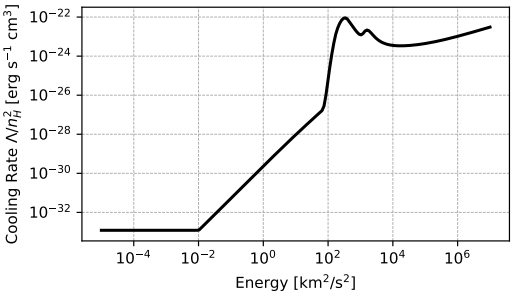

(f) $\rho = 10^{12}\,\mathrm{M}_\odot/\mathrm{kpc}^3$ & $G_0 = 0$

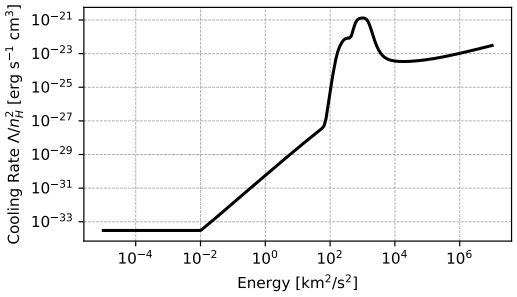

(g) $\rho = 10^{15}\,\mathrm{M}_\odot/\mathrm{kpc}^3$ & $G_0 = 0$

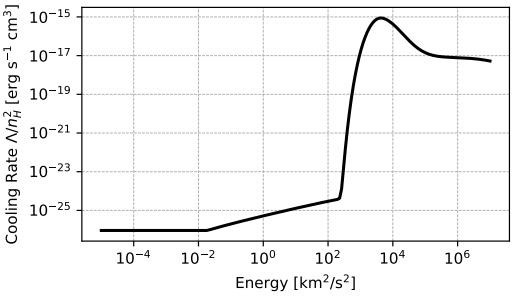

(h) $\rho = 10^{21}\,\mathrm{M}_\odot/\mathrm{kpc}^3$ & $G_0 = 0$

Figure 4.2: Cooling rate for different densities ρ and $G_0 = 0$

4.2.2 Effect of Varying G_0

Figure 4.3 shows the cooling rate, Λ/n_H^2, in units of erg s^{-1} cm^3, with a constant gas density of $\rho = 10^6\,M_\odot/kpc^3$. The far-ultraviolet (FUV) radiation intensity, G_0, is varied to study its effect on the cooling rate. For G_0 values below 10^6, the cooling rate is almost identical to the case where $G_0 = 0$. However, when G_0 reaches 10^9, the cooling rate turns positive at low energy levels. As G_0 increases further, the magnitude of this positive cooling rate also grows.

At very high G_0 values, such as 10^{15}, the cooling rate shows noticeable changes up to an energy of about $10^3\,km^2/s^2$. This corresponds to a temperature of approximately $20,000\,K$, above which Grackle sets the photoelectric heating efficiency factor ϵ to zero. These results emphasize how high G_0 values significantly affect the cooling processes in minihalos, especially at low energy levels where photoelectric heating is the main factor.

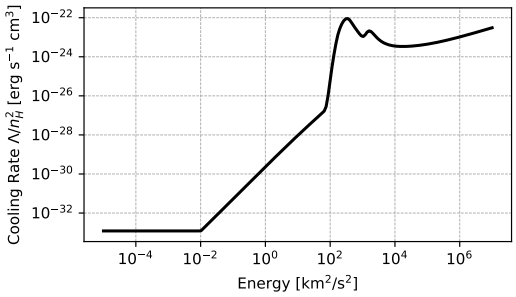

(a) $\rho = 10^6\,\mathrm{M}_\odot/\mathrm{kpc}^3$ & $G_0 = 10^0$

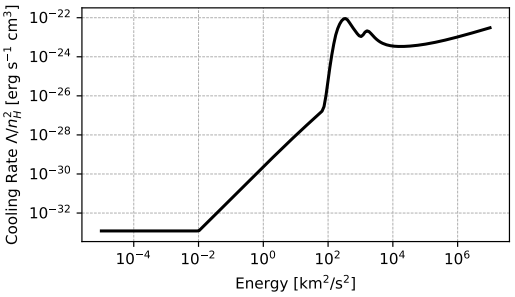

(b) $\rho = 10^6\,\mathrm{M}_\odot/\mathrm{kpc}^3$ & $G_0 = 10^3$

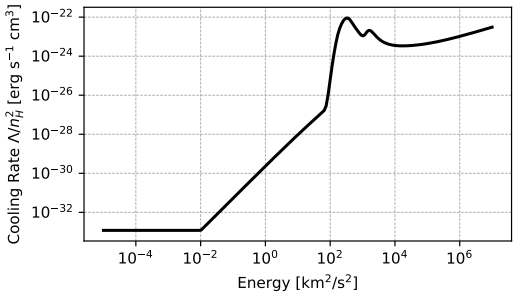

(c) $\rho = 10^6\,\mathrm{M}_\odot/\mathrm{kpc}^3$ & $G_0 = 10^6$

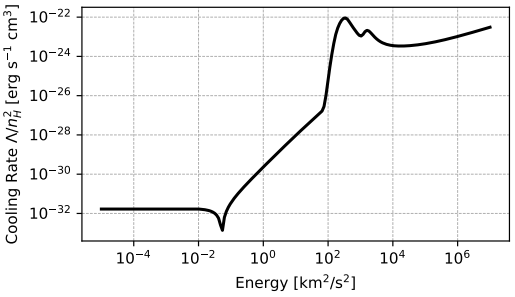

(d) $\rho = 10^6\,\mathrm{M}_\odot/\mathrm{kpc}^3$ & $G_0 = 10^9$

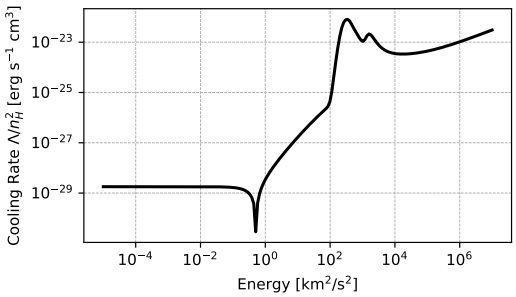

(e) $\rho = 10^6\,\mathrm{M}_\odot/\mathrm{kpc}^3$ & $G_0 = 10^{12}$

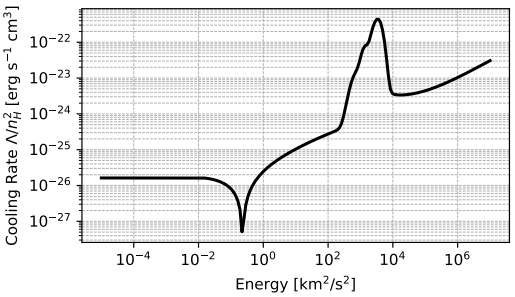

(f) $\rho = 10^6\,\mathrm{M}_\odot/\mathrm{kpc}^3$ & $G_0 = 10^{15}$

Figure 4.3: Cooling rate for different values of G_0 and $\rho = 10^6\,\mathrm{M}_\odot/\mathrm{kpc}^3$

4.2.3 Combined Variation of Density and G_0

This subsection analyzes how the combined variation of gas density and FUV radiation intensity (G_0) affects the cooling rate. Figure 4.3 shows the cooling rate for different G_0 values at a density of $\rho = 10^6\,\mathrm{M}_\odot/\mathrm{kpc}^3$, while Figure 4.4 represents

the cooling rate at a lower density of $\rho = 10^3\,\mathrm{M}_\odot/\mathrm{kpc}^3$. A key observation is that at the lower density ($\rho = 10^3\,\mathrm{M}_\odot/\mathrm{kpc}^3$), changes in the cooling rate start appearing at $G_0 = 10^3$. In contrast, at the higher density ($\rho = 10^6\,\mathrm{M}_\odot/\mathrm{kpc}^3$), noticeable changes are only seen at $G_0 = 10^9$.

This significant difference shows that photoelectric heating becomes effective at much lower G_0 values for low-density gas. For example, the effects of photoelectric heating observed at $G_0 = 10^9$ for $\rho = 10^6\,\mathrm{M}_\odot/\mathrm{kpc}^3$ occur about six orders of magnitude earlier (around $G_0 = 10^3$) for $\rho = 10^3\,\mathrm{M}_\odot/\mathrm{kpc}^3$. This indicates that the influence of G_0 is inversely related to gas density: lower densities respond more strongly to radiation.

As G_0 increases and the photoelectric heating effect becomes stronger, it significantly modifies the overall cooling rate. At very high G_0 values, the cooling rate begins to diverge or flatten, suggesting a potential convergence issue in the calculations. This behavior requires further investigation, as it might arise from numerical challenges when modeling extreme radiation conditions.

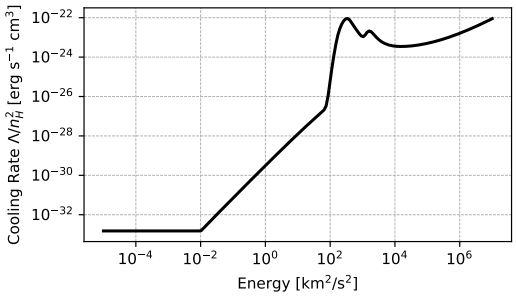

(a) $\rho = 10^3\,\mathrm{M}_\odot/\mathrm{kpc}^3$ & $G_0 = 10^0$

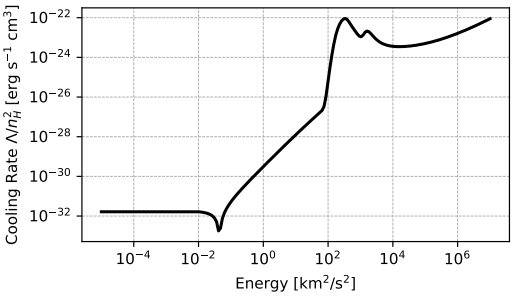

(b) $\rho = 10^3\,\mathrm{M}_\odot/\mathrm{kpc}^3$ & $G_0 = 10^3$

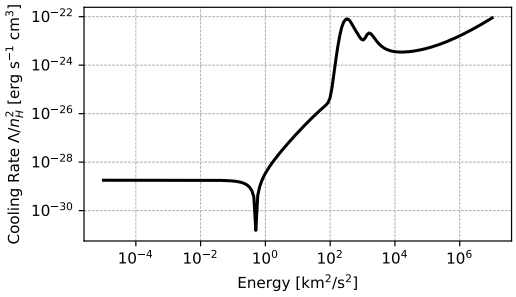

(c) $\rho = 10^3\,\mathrm{M}_\odot/\mathrm{kpc}^3$ & $G_0 = 10^6$

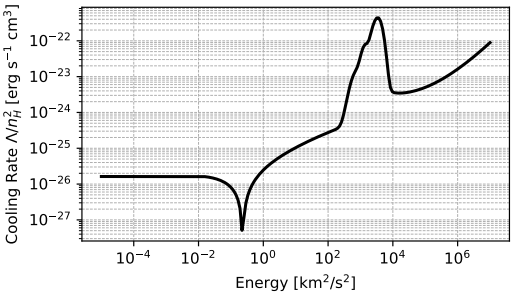

(d) $\rho = 10^3\,\mathrm{M}_\odot/\mathrm{kpc}^3$ & $G_0 = 10^9$

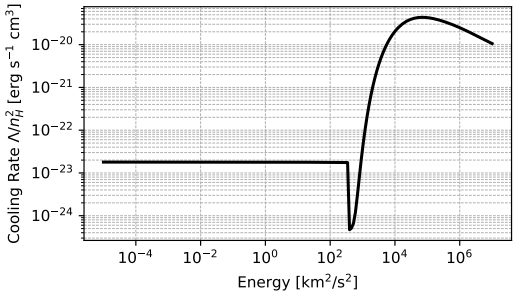

(e) $\rho = 10^3\,\mathrm{M}_\odot/\mathrm{kpc}^3$ & $G_0 = 10^{12}$

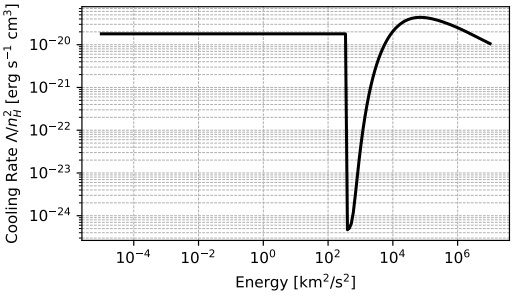

(f) $\rho = 10^3\,\mathrm{M}_\odot/\mathrm{kpc}^3$ & $G_0 = 10^{15}$

Figure 4.4: Cooling rate for different values of G_0 and $\rho = 10^3\,\mathrm{M}_\odot/\mathrm{kpc}^3$

4.3 Extrapolation

4.3.1 Extrapolating Low Densities

As shown in Figure 4.5, the cooling rate at very low densities follows a linear relationship. Since extremely low densities, which are relevant in our simulations, cannot be directly computed using Grackle, an extrapolation is necessary. By examining the behavior of Λ/ρ, as plotted in Figure 4.6, it becomes evident that this quantity becomes independent of density in the low-density regime.

Neglecting the effects of the cosmic microwave background (CMB) temperature floor, it is possible to derive an analytical formula for Λ/ρ that remains valid across all densities:

$$\Lambda/\rho = -2.39 \cdot 10^{-4} \cdot E, \tag{4.1}$$

where E represents the specific energy in $(\mathrm{km/s})^2$ and Λ/ρ is expressed in units of $(\mathrm{km/s})^2\,\mathrm{kpc}^3\,\mathrm{M}_\odot/\mathrm{Gyr}$.

The standard deviation of the slope in this linear relationship is:

$$\sigma = 5.74 \cdot 10^{-11}.$$

To account for photoelectric heating, as described by Wolfire et al. [28], an additional term for heating, Γ, can be included for temperatures below 20,000 K. This heating term can be computed using Equation 2.26, ensuring that both cooling and heating effects are accurately incorporated in the extrapolated regime. This adjustment allows for a better representation of the thermal processes in the low-density environments of the minihalo.

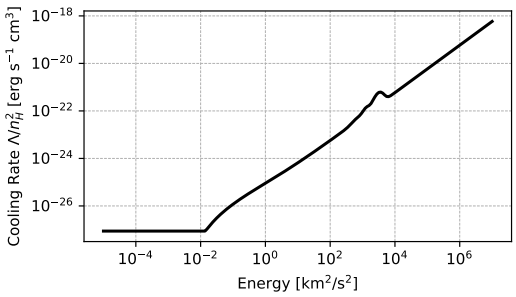

(a) $\rho = 10^{-1}\,\mathrm{M}_\odot/\mathrm{kpc}^3$ & $G_0 = 0$

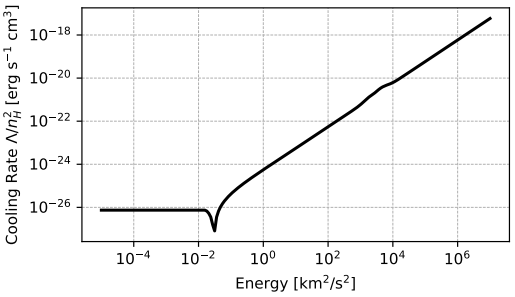

(b) $\rho = 10^{-2}\,\mathrm{M}_\odot/\mathrm{kpc}^3$ & $G_0 = 0$

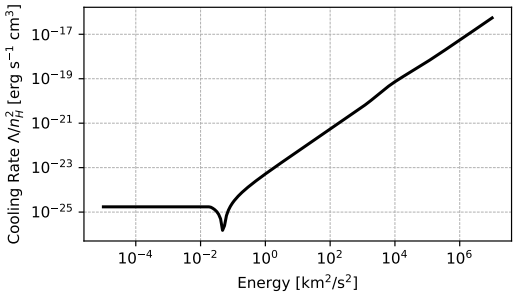

(c) $\rho = 10^{-3}\,\mathrm{M}_\odot/\mathrm{kpc}^3$ & $G_0 = 0$

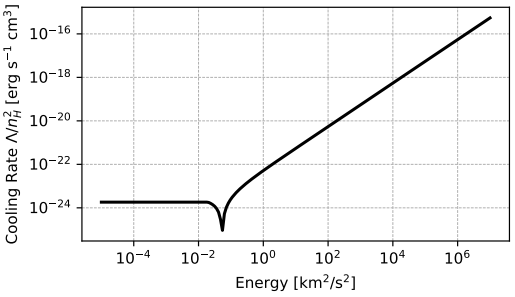

(d) $\rho = 10^{-4}\,\mathrm{M}_\odot/\mathrm{kpc}^3$ & $G_0 = 0$

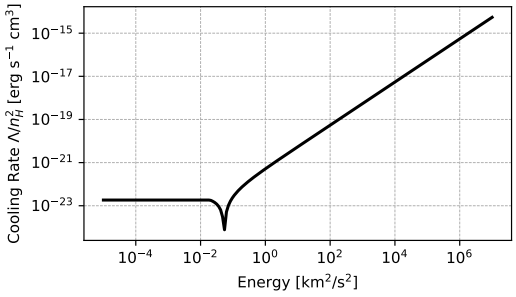

(e) $\rho = 10^{-5}\,\mathrm{M}_\odot/\mathrm{kpc}^3$ & $G_0 = 0$

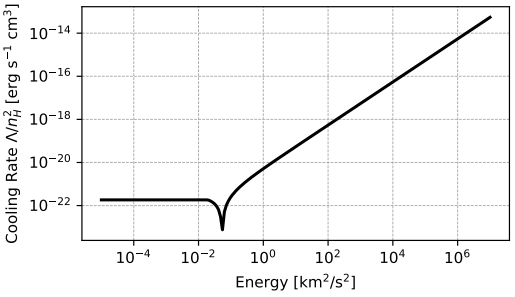

(f) $\rho = 10^{-6}\,\mathrm{M}_\odot/\mathrm{kpc}^3$ & $G_0 = 0$

Figure 4.5: Cooling rate for different values with a low density and $G_0 = 0$

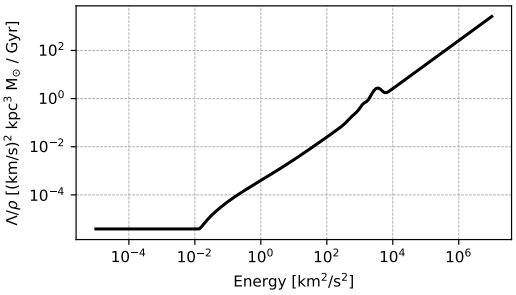

(a) $\rho = 10^{-1}\,\mathrm{M}_\odot/\mathrm{kpc}^3$ & $G_0 = 0$

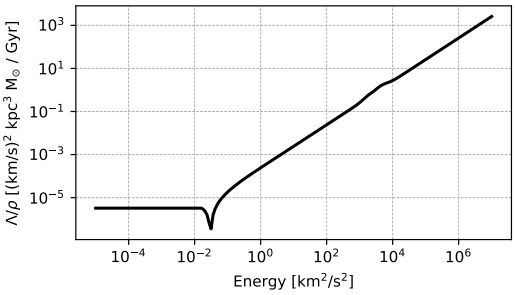

(b) $\rho = 10^{-2}\,\mathrm{M}_\odot/\mathrm{kpc}^3$ & $G_0 = 0$

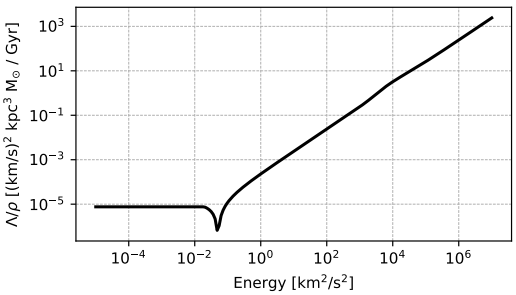

(c) $\rho = 10^{-3}\,\mathrm{M}_\odot/\mathrm{kpc}^3$ & $G_0 = 0$

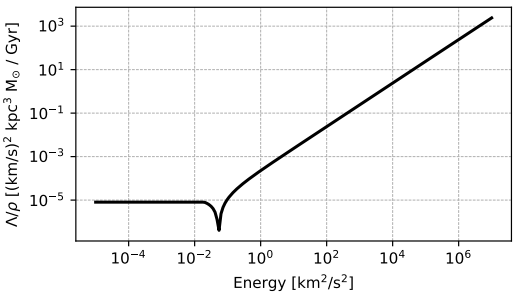

(d) $\rho = 10^{-4}\,\mathrm{M}_\odot/\mathrm{kpc}^3$ & $G_0 = 0$

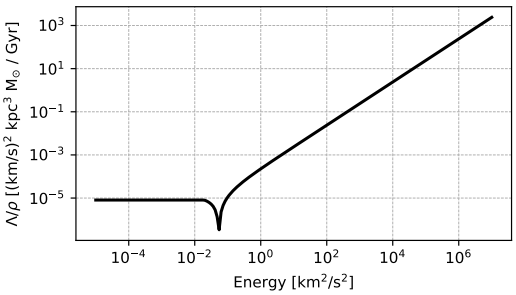

(e) $\rho = 10^{-5}\,\mathrm{M}_\odot/\mathrm{kpc}^3$ & $G_0 = 0$

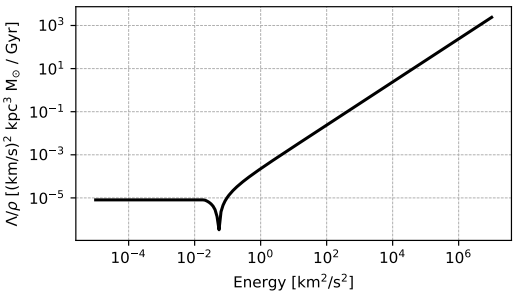

(f) $\rho = 10^{-6}\,\mathrm{M}_\odot/\mathrm{kpc}^3$ & $G_0 = 0$

Figure 4.6: Λ/ρ in $(\mathrm{km/s})^2\ \mathrm{kpc}^3\ \mathrm{M}_\odot$ / Gyr for different values with a low density and $G_0 = 0$

4.3.2 Extrapolating Internal Energy Values

The data for internal energy E and the corresponding values of Λ/ρ were first transformed into a logarithmic scale to analyze their relationship in log-log space.

This transformation was done using the formulas:

$$\text{log\_energy} = \log_{10}(E), \quad \text{log\_lod} = \log_{10}(|\text{LOD}|) \tag{4.2}$$

where E represents internal energy and LOD represents Λ/ρ At the lower and upper ends of the data range, linear regression was applied to find the slope and intercept in the log-log space. For the lower boundary values (E_{low}), the relationship was fitted with the equation:

$$\text{log\_lod} = m_{\text{low}} \cdot \text{log\_energy} + b_{\text{low}} \tag{4.3}$$

Similarly, for the upper boundary values (E_{high}), the equation used was:

$$\text{log\_lod} = m_{\text{high}} \cdot \text{log\_energy} + b_{\text{high}} \tag{4.4}$$

Using the parameters $m_{\text{low}}, b_{\text{low}}, m_{\text{high}}$, and b_{high} from the fits, the extrapolated Λ/ρ values were calculated for energy ranges outside the available data. The extrapolated values were given by:

$$\text{LOD}_{\text{low}} = 10^{(m_{\text{low}} \cdot \log_{10}(E) + b_{\text{low}})} \tag{4.5}$$

$$\text{LOD}_{\text{high}} = 10^{(m_{\text{high}} \cdot \log_{10}(E) + b_{\text{high}})} \tag{4.6}$$

Figure 4.7 shows the extrapolated behavior of Λ/ρ for a density of $\rho = 10^6\ \text{M}_\odot/\text{kpc}^3$ and $G_0 = 9$. The extrapolation provides reliable estimates for cooling rates at internal energies outside the range computed directly by Grackle.

4.4 Comparison with Other Studies

Figure 4.8 shows the cooling rate, Λ/n_H^2, in units of erg s^{-1} cm^3 as a function of temperature T in Kelvin. Comparing Figure 4.8 with Figure 4.9, which presents a similar plot from Thoul's study [36], reveals that the total cooling rates are nearly identical.

Looking at Figure 4.1 from this work and Thoul's plot in Figure 4.9 shows a strong agreement between the cooling rates and the contributions of individual

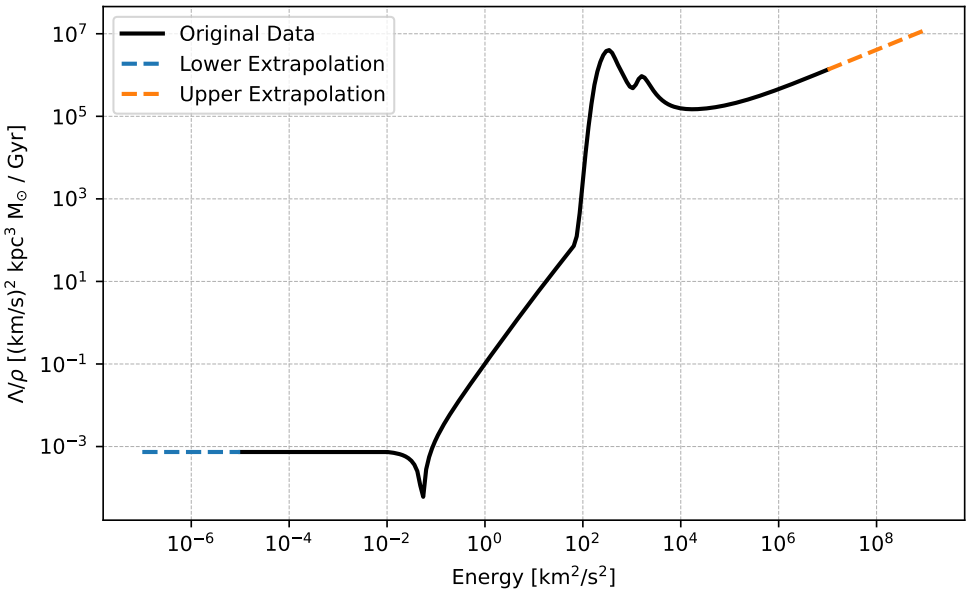

Figure 4.7: Extrapolation of Λ/ρ for $\rho = 10^6\,\mathrm{M}_\odot/\mathrm{kpc}^3$ & $G_0 = 9$

processes across the temperature range. Both figures highlight the same dominant mechanisms in similar temperature ranges, providing solid validation for the results presented in this study.

The total cooling rate matches almost perfectly, showing that the combined effect of all individual processes is accurately captured. The two main peaks, corresponding to collisional excitation and collisional ionization, appear in both studies. The excitation peak in Thoul's results is slightly more pronounced. Similarly, the free-free cooling (bremsstrahlung) displays the same upward trend at high temperatures, confirming its importance in hot and dense environments.

Some small differences can be seen, particularly in the strength of the collisional excitation and ionization peaks, which are slightly higher in Thoul's results. These differences may come from variations in atomic data or numerical methods used in the two studies. Despite these minor discrepancies, the overall patterns and key features remain consistent, demonstrating the reliability of the models and methods used here.

This strong agreement shows the robustness of the cooling and heating rate

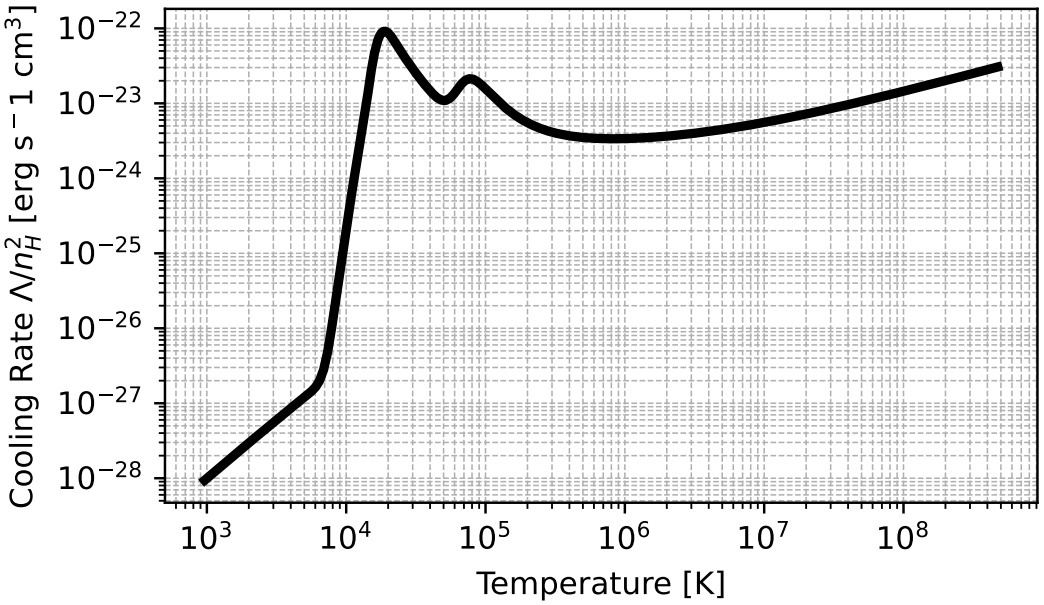

Figure 4.8: Λ/n_H^2 in units of erg s^{-1} cm^3 plottet against Temperture in Kelvin for $\rho = 1.5 \cdot 10^7\,\mathrm{M}_\odot/\mathrm{kpc}^3$ & $G_0 = 0$

calculations performed in this study. It also confirms that the Grackle library is well-suited for modeling the thermal and chemical evolution of minihalos, as it successfully reproduces established results from earlier research.

Figure 4.10 from Barkana & Loeb [37] shows the cooling rates as a function of temperature for a primordial gas made up of atomic hydrogen and helium, including molecular hydrogen. The cooling rate Λ/n_H^2, given in erg s^{-1} cm^3, provides a direct comparison to the results of this study.

Similar to our findings, their plot shows characteristic peaks caused by collisional excitation of hydrogen and helium, mainly at temperatures of about 10^4 K and 10^5 K, respectively. However, the inclusion of molecular hydrogen cooling in Barkana & Loeb introduces an extra feature at lower temperatures ($T \sim 10^3$ K). This feature is not seen in our results because molecular hydrogen processes were excluded due to the simplified chemical network used in this study.

Even with this small difference, the overall shape of the cooling curve matches well with the results presented in this thesis.

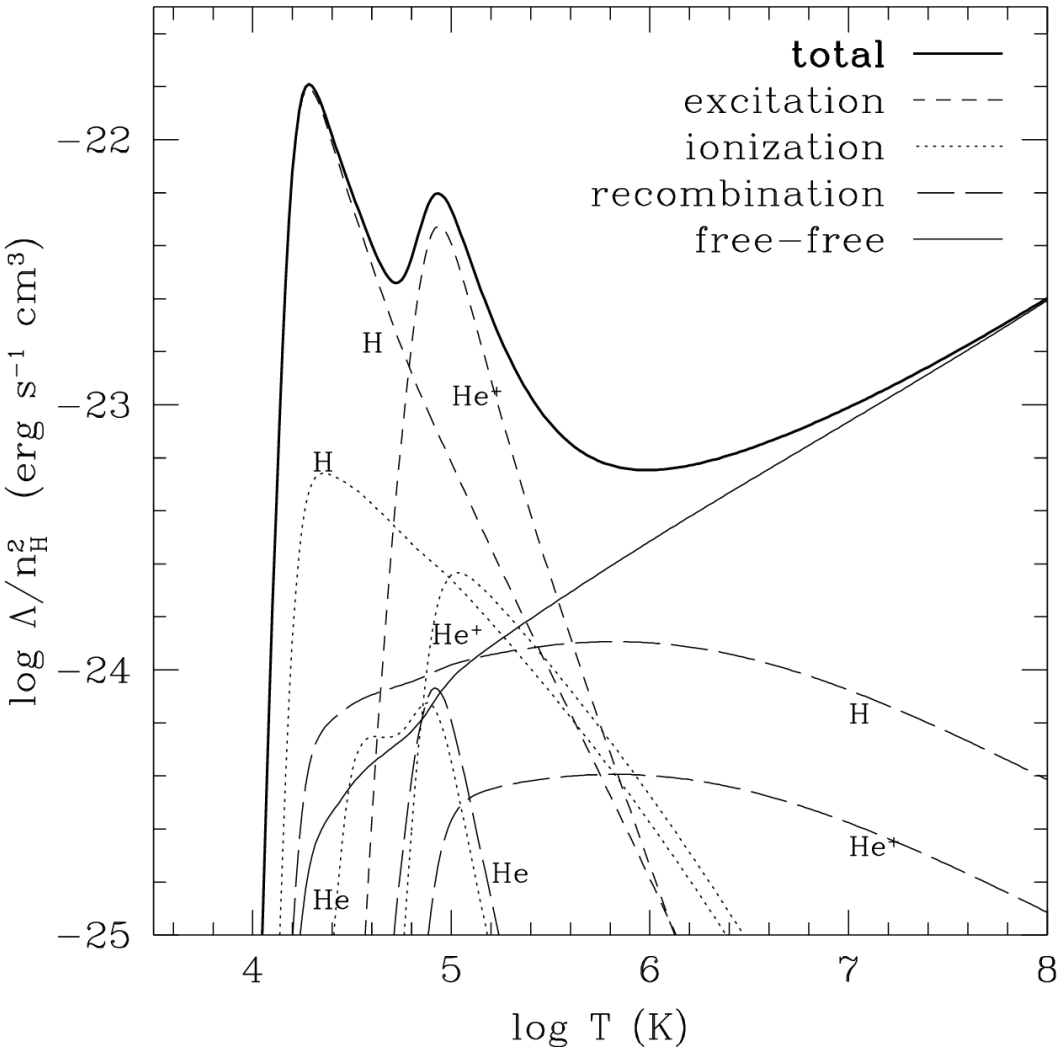

Figure 4.9: Plot from Figure 1 of [36]

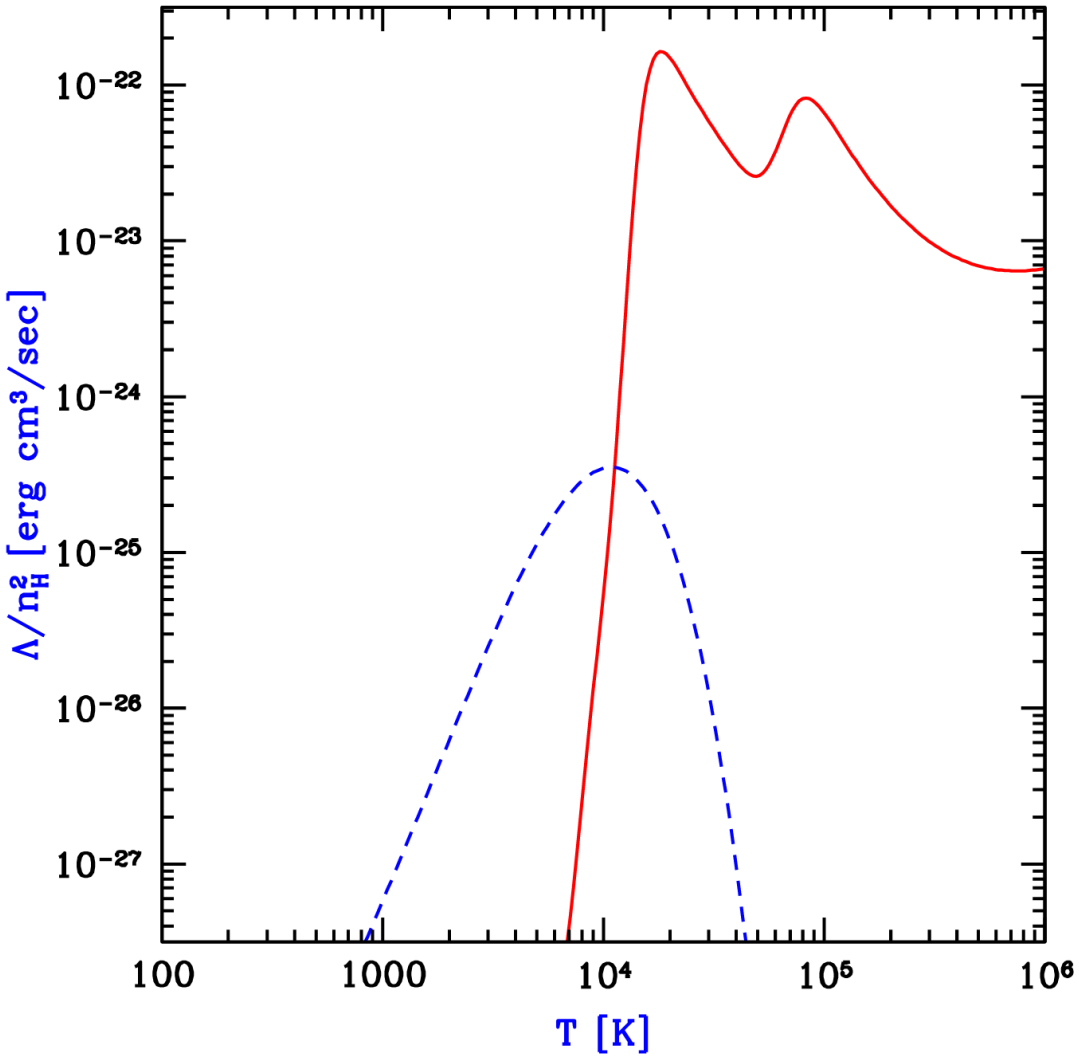

Figure 4.10: Cooling rates as a function of temperature for a primordial gas composed of atomic hydrogen and helium, including molecular hydrogen, in the absence of external radiation. The hydrogen number density is assumed to be $n_H = 0.045\,\mathrm{cm}^{-3}$, corresponding to the mean density of virialized halos at $z = 10$. The plotted quantity Λ/n_H^2 (in units of erg s^{-1} cm^3) is roughly independent of density unless $n_H \gg 10\,\mathrm{cm}^{-3}$. The solid line represents the cooling curve for atomic gas, with characteristic peaks from collisional excitation of H I and He II. The dashed line includes additional molecular cooling contributions, assuming a molecular hydrogen abundance of 0.1% of n_H (adapted from Barkana & Loeb [37]).

5 Conclusion and Outlook

This study investigated the cooling and heating processes within minihalos, focusing on the influence of varying gas densities and FUV radiation intensities (G_0). Several key findings were observed. At low temperatures, recombination cooling was the dominant mechanism, effectively reducing the thermal energy of the gas. In intermediate temperature ranges, collisional excitation and ionization contributed significantly to cooling, while at higher temperatures, bremsstrahlung emerged as the primary cooling process. The cooling rate displayed distinct trends across density regimes, becoming density-independent at low densities and increasing substantially at higher densities due to enhanced collisional interactions. Photoelectric heating had a notable impact, especially at high G_0 values, with its effects being more pronounced in low-density environments. The results align well with prior studies, such as those by Thoul [36] and Barkana & Loeb [37], demonstrating the robustness of the methods and models used in this work.

The parameter space explored in this study is well-suited for the conditions typical of minihalos. However, the framework established here can be extended to other astrophysical scenarios by modifying the input parameters and chemical networks. For example, incorporating metallicity-dependent cooling or introducing more complex radiation fields could enable the application of these methods to star-forming regions or galaxy clusters.

Future work could leverage the flexibility of the Grackle library to explore these extensions. Incorporating advanced parameter configurations could help study the coupled evolution of gas dynamics and thermal processes in various astrophysical systems. The pre-calculated parameter grids generated in this study could serve as a foundation for broader applications. These steps would further enhance the understanding of thermal and chemical processes in a wide range of scenarios, from the early universe to modern galactic ecosystems.

6 Bibliography

[1] N. Aghanim et al. "Planck2018 results: VI. Cosmological parameters". In: *Astronomy amp; Astrophysics* 641 (Sept. 2020), A6. ISSN: 1432-0746. DOI: 10.1051/0004-6361/201833910. URL: http://dx.doi.org/10.1051/0004-6361/201833910.

[2] Vera C. Rubin, W. Kent Ford, and Norbert Thonnard. "Rotational properties of 21 SC galaxies with a large range of luminosities and radii, from NGC 4605/GC 6543". In: *The Astrophysical Journal* 238 (1980), pp. 471–487. DOI: 10.1086/158003. URL: https://ui.adsabs.harvard.edu/abs/1980ApJ...238..471R/abstract.

[3] Douglas Clowe et al. "A Direct Empirical Proof of the Existence of Dark Matter". In: *The Astrophysical Journal* 648.2 (Aug. 2006), pp. L109–L113. ISSN: 1538-4357. DOI: 10.1086/508162. URL: http://dx.doi.org/10.1086/508162.

[4] Volker Springel et al. "Simulations of the formation, evolution and clustering of galaxies and quasars". In: *Nature* 435.7042 (June 2005), pp. 629–636. DOI: 10.1038/nature03597. URL: https://doi.org/10.1038/nature03597.

[5] Volker Springel et al. *The Millennium Simulation Project*. https://wwwmpa.mpa-garching.mpg.de/galform/virgo/millennium/. Accessed: 2024-11-21. 2005. URL: https://wwwmpa.mpa-garching.mpg.de/galform/virgo/millennium/.

[6] Julio F. Navarro, Carlos S. Frenk, and Simon D. M. White. "The Structure of Cold Dark Matter Halos". In: *The Astrophysical Journal* 462 (May 1996), p. 563. ISSN: 1538-4357. DOI: 10.1086/177173. URL: http://dx.doi.org/10.1086/177173.

[7] Sean Tulin and Hai-Bo Yu. "Dark matter self-interactions and small scale structure". In: *Physics Reports* 730 (Feb. 2018), pp. 1–57. ISSN: 0370-1573. DOI: 10.1016/j.physrep.2017.11.004. URL: http://dx.doi.org/10.1016/j.physrep.2017.11.004.

[8] Mark Vogelsberger et al. "Dwarf galaxies in CDM and SIDM with baryons: observational probes of the nature of dark matter". In: *Monthly Notices of the Royal Astronomical Society* 444.4 (Sept. 2014), pp. 3684–3698. ISSN: 0035-8711. DOI: 10.1093/mnras/stu1713. URL: http://dx.doi.org/10.1093/mnras/stu1713.

[9] Jonathan L Feng et al. "Hidden charged dark matter". In: *Journal of Cosmology and Astroparticle Physics* 2009.07 (July 2009), pp. 004–004. ISSN: 1475-7516. DOI: 10.1088/1475-7516/2009/07/004. URL: http://dx.doi.org/10.1088/1475-7516/2009/07/004.

[10] Matteo Viel et al. "Warm dark matter as a solution to the small scale crisis: New constraints from high redshift Lyman-α forest data". In: *Phys. Rev. D* 88 (4 Aug. 2013), p. 043502. DOI: 10.1103/PhysRevD.88.043502. URL: https://link.aps.org/doi/10.1103/PhysRevD.88.043502.

[11] Max Tegmark et al. "How Small Were the First Cosmological Objects?" In: *The Astrophysical Journal* 474.1 (Jan. 1997), pp. 1–12. ISSN: 1538-4357. DOI: 10.1086/303434. URL: http://dx.doi.org/10.1086/303434.

[12] Volker Bromm, Paolo S. Coppi, and Richard B. Larson. "The Formation of the First Stars. I. The Primordial Star-forming Cloud". In: *The Astrophysical Journal* 564 (2002), pp. 23–51. DOI: 10.1086/323947. URL: https://iopscience.iop.org/article/10.1086/323947.

[13] Z Haiman. "Formation of the first stars and quasars". In: *Advances in Space Research* 23.5–6 (Jan. 1999), pp. 915–924. ISSN: 0273-1177. DOI: 10.1016/s0273-1177(99)00216-1. URL: http://dx.doi.org/10.1016/S0273-1177(99)00216-1.

[14] ESA, Planck Collaboration, and adapted by L. Steenblik Hwang. *Cosmic Timeline: From the Big Bang to Today*. Image courtesy of ESA and the Planck Collaboration, adapted by L. Steenblik Hwang. Accessed: 27 Novem-

ber 2024. 2024. URL: https://www.esa.int/var/esa/storage/images/esa_multimedia/images/2013/03/planck_history_of_universe/12584080-5-eng-GB/Planck_history_of_Universe_pillars.jpg.

[15] Scott Dodelson. *Modern Cosmology*. Academic Press, 2003.

[16] Marta Volonteri. "Formation of supermassive black holes". In: *The Astronomy and Astrophysics Review* 18.3 (Apr. 2010), pp. 279–315. ISSN: 1432-0754. DOI: 10.1007/s00159-010-0029-x. URL: http://dx.doi.org/10.1007/s00159-010-0029-x.

[17] Luca Ciotti and Jeremiah P. Ostriker. "Radiative Feedback from Massive Black Holes in Elliptical Galaxies: AGN Flaring and Central Starburst Fueled by Recycled Gas". In: *The Astrophysical Journal* 665.2 (Aug. 2007), pp. 1038–1056. ISSN: 1538-4357. DOI: 10.1086/519833. URL: http://dx.doi.org/10.1086/519833.

[18] Gregory S. Novak, Jeremiah P. Ostriker, and Luca Ciotti. "FEEDBACK FROM CENTRAL BLACK HOLES IN ELLIPTICAL GALAXIES: TWO-DIMENSIONAL MODELS COMPARED TO ONE-DIMENSIONAL MODELS". In: *The Astrophysical Journal* 737.1 (July 2011), p. 26. ISSN: 1538-4357. DOI: 10.1088/0004-637x/737/1/26. URL: http://dx.doi.org/10.1088/0004-637X/737/1/26.

[19] Zoltan Haiman, Anne A. Thoul, and Abraham Loeb. "Cosmological Formation of Low-Mass Objects". In: *The Astrophysical Journal* 464 (June 1996), p. 523. ISSN: 1538-4357. DOI: 10.1086/177343. URL: http://dx.doi.org/10.1086/177343.

[20] Bruce T. Draine. *Physics of the Interstellar and Intergalactic Medium*. Princeton, NJ: Princeton University Press, 2011. ISBN: 978-0-691-12214-4.

[21] Daniel Wolf Savin et al. "Rate Coefficient for H+ + H2(X1g+, = 0, J = 0) → H(1s) + H2+ Charge Transfer and Some Cosmological Implications". In: *The Astrophysical Journal* 606.2 (Apr. 2004), pp. L167–L170. ISSN: 1538-4357. DOI: 10.1086/421108. URL: http://dx.doi.org/10.1086/421108.

[22] Tom Abel, Greg L. Bryan, and Michael L. Norman. "The Formation of the First Star in the Universe". In: *Science* 295.5552 (Jan. 2002), pp. 93–98. DOI: 10.1126/science.295.5552.93. eprint: arXiv:astro-ph/0112088. URL: https://ui.adsabs.harvard.edu/abs/2002Sci...295...93A/abstract.

[23] Francesco Palla, E. E. Salpeter, and Steven W. Stahler. "Primordial Star Formation: The Role of Molecular Hydrogen". In: *The Astrophysical Journal* 271 (Aug. 1983), pp. 632–641. DOI: 10.1086/161231. URL: https://ui.adsabs.harvard.edu/abs/1983ApJ...271..632P/abstract.

[24] Simon Glover. "Chemistry and Cooling in Metal-Free and Metal-Poor Gas". In: *First Stars III: First Stars II Conference*. Vol. 990. AIP Conference Proceedings. Mar. 2008, pp. 25–29. DOI: 10.1063/1.2905558. URL: https://ui.adsabs.harvard.edu/abs/2008AIPC..990...25G/abstract.

[25] Matthew J. Turk et al. "Effects of Varying the Three-body Molecular Hydrogen Formation Rate in Primordial Star Formation". In: *The Astrophysical Journal* 726.1 (Jan. 2011), p. 55. DOI: 10.1088/0004-637X/726/1/55. URL: https://ui.adsabs.harvard.edu/abs/2011ApJ...726...55T/abstract.

[26] François Lique. "Revisited study of the ro-vibrational excitation of H2 by H: towards a revision of the cooling of astrophysical media". In: *Monthly Notices of the Royal Astronomical Society* 453.1 (2015), pp. 810–818. DOI: 10.1093/mnras/stv1683. URL: https://academic.oup.com/mnras/article/453/1/810/1752438.

[27] Donald E. Osterbrock and Gary J. Ferland. *Astrophysics of Gaseous Nebulae and Active Galactic Nuclei*. 2nd. Sausalito, CA: University Science Books, 2006. ISBN: 978-1-891389-34-8.

[28] Mark G. Wolfire et al. "The Neutral Atomic Phases of the Interstellar Medium". In: *The Astrophysical Journal* 443 (Apr. 1995), pp. 152–168. DOI: 10.1086/175510. URL: https://doi.org/10.1086/175510.

[29] Britton D. Smith et al. "grackle: a chemistry and cooling library for astrophysics". In: *Monthly Notices of the Royal Astronomical Society* 466.2 (Dec. 2016), pp. 2217–2234. ISSN: 1365-2966. DOI: 10.1093/mnras/stw3291. URL: http://dx.doi.org/10.1093/mnras/stw3291.

[30] John H. Black. “The Physical State of Primordial Intergalactic Clouds”. In: *Monthly Notices of the Royal Astronomical Society* 197 (1981). Available via NASA Astrophysics Data System (ADS), pp. 553–563. URL: https://articles.adsabs.harvard.edu/pdf/1981MNRAS.197..553B.

[31] Renyue Cen. “A Hydrodynamic Approach to Cosmology: Methodology”. In: *The Astrophysical Journal Supplement Series* 78 (Feb. 1992), pp. 341–364. DOI: 10.1086/191630.

[32] Paul R. Shapiro and Hyesung Kang. “Hydrogen Molecules and the Radiative Cooling of Pregalactic Shocks”. In: *The Astrophysical Journal* 318 (1987), pp. 32–65. URL: https://articles.adsabs.harvard.edu/pdf/1987ApJ...318...32S.

[33] Tom Abel et al. “Modeling Primordial Gas in Numerical Cosmology”. In: *New Astronomy* 2 (1997), pp. 181–207. DOI: 10.1016/S1384-1076(97)00010-9. URL: https://www.sciencedirect.com/science/article/pii/S1384107697000109.

[34] G. J. Ferland et al. “Anisotropic Line Emission and the Geometry of the Broad-Line Region in Active Galactic Nuclei”. In: *The Astrophysical Journal* 387 (Mar. 1992), pp. 95–108. DOI: 10.1086/171070. URL: https://ui.adsabs.harvard.edu/abs/1992ApJ...387...95F/abstract.

[35] Lam Hui and Nickolay Y. Gnedin. “Equation of State of the Photoionized Intergalactic Medium”. In: *Monthly Notices of the Royal Astronomical Society* 292 (1997), pp. 27–42. DOI: 10.1093/mnras/292.1.27. URL: https://ui.adsabs.harvard.edu/abs/1997MNRAS.292...27H/abstract.

[36] Anne A. Thoul and David H. Weinberg. “Hydrodynamic Simulations of Galaxy Formation. I. Dissipation and the Maximum Mass of Galaxies”. In: *The Astrophysical Journal* 421 (1994), pp. 456–472. DOI: 10.1086/175455. URL: https://arxiv.org/abs/astro-ph/9410009.

[37] Rennan Barkana and Abraham Loeb. “In the Beginning: The First Sources of Light and the Reionization of the Universe”. In: *arXiv e-prints* (2001). Version 3, 11 May 2001. eprint: astro-ph/0010468. URL: https://arxiv.org/abs/astro-ph/0010468.

Ehrenwörtliche Erklärung

Erklärung nach § 39 (15) Prüfungsordnung 2020 für den BAMA-Studiengang Physik

Hiermit erkläre ich, dass ich die Arbeit selbstständig und ohne Benutzung anderer als der angegebenen Quellen und Hilfsmittel verfasst habe. Alle Stellen der Arbeit, die wörtlich oder sinngemäß aus Veröffentlichungen oder aus anderen fremden Texten entnommen wurden, sind von mir als solche kenntlich gemacht worden. Ferner erkläre ich, dass die Arbeit nicht – auch nicht auszugsweise – für eine andere Prüfung verwendet wurde.

Ort, Datum: Unterschrift: